Inorganic Chemistry

pubs.acs.org/IC

Article

# Enhancement of Oxidative Asynchronicity in Hydrogen Atom Abstraction by a Mononuclear Mn(III)-OMe Complex via Protonation and Sodium Ion Binding

Mofijul Molla, Anannya Saha, Nirmalya Podder, Suman K. Barman, and Sukanta Mandal*

Cite This: *Inorg. Chem.* 2026, 65, 8465−8480

Read Online

ACCESS | Metrics & More | Article Recommendations | Supporting Information

**ABSTRACT:** This paper reports the preparation of three mononuclear Mn(III) complexes supported by a pentadentate, dianionic $N_4O$ donor ligand, $L^{2-}$ ($H_2L$ = 2-((2-((2-hydroxybenzyl)(methyl)amino)ethyl)(methyl)amino)-*N*-(quinolin-8-yl)acetamide): $[Mn^{III}(L)(OMe)]$ ($\mathbf{1}^{OMe}$), $\{Na[Mn^{III}(L)(OMe)]\}^{1+}$ ($\mathbf{Na^+1^{OMe}}$), and $[Mn^{III}(L)(MeOH)]^{1+}$ ($\mathbf{1}^{MeOH+}$). The complexes were characterized by analytical and spectroscopic techniques, including magnetic measurements, X-ray crystallography for $\mathbf{Na^+1^{OMe}}$ and $\mathbf{1}^{MeOH+}$, and $^{23}$Na NMR spectroscopy for $\mathbf{Na^+1^{OMe}}$. Complexes $\mathbf{1}^{OMe}$ and $\mathbf{Na^+1^{OMe}}$ contain a terminal $Mn^{III}$−OMe unit, while $\mathbf{Na^+1^{OMe}}$ forms a $Na^+$ Lewis acid adduct through interaction with methoxide and phenoxide oxygen atoms. Complex $\mathbf{1}^{MeOH+}$ features a terminal methanol ligand, serving as the protonated analog of $[Mn^{III}(L)(OMe)]$. These complexes abstract hydrogen atoms from 4-R-2,6-di-*tert*-butylphenols (R = OMe, Me, H, Br), with rates increasing in the order $\mathbf{1}^{OMe}$ < $\mathbf{Na^+1^{OMe}}$ < $\mathbf{1}^{MeOH+}$, consistent with anodically shifted $Mn^{III}/Mn^{II}$ redox potentials. Hammett and Bell−Evans−Polanyi analyses, large negative $\Delta S^{\ddagger}$ values, and kinetic isotope effects support an apparent concerted proton−electron transfer (CPET) pathway. However, nonzero slopes (−0.262 to −0.286) in Marcus-type plots indicate an oxidatively asynchronous CPET pathway. Density functional theory calculations, including electrostatic potential mapping, asynchronicity factor ($\eta$) evaluation, and free-energy analysis of electron- and proton-transfer steps, further support the ET-dominated concerted pathway. The study reveals that binding of $H^+$ or $Na^+$ to the Mn(III)-OMe complex increases the oxidative asynchronicity factor, facilitating phenolic O−H bond activation during hydrogen-atom transfer.

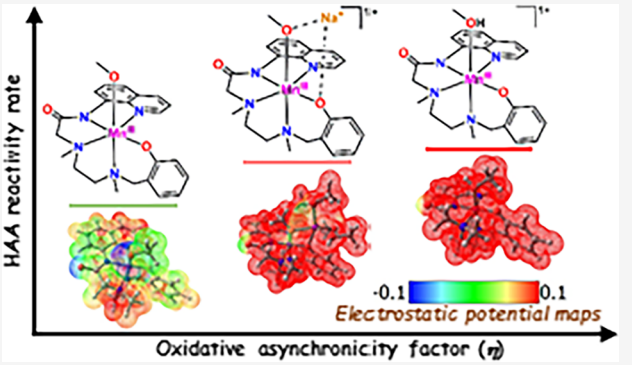


Downloaded via INDIAN INST OF TECH KHARAGPUR on April 20, 2026 at 14:42:07 (UTC).
See https://pubs.acs.org/sharingguidelines for options on how to legitimately share published articles.

## INTRODUCTION

Manganese (Mn) is an essential trace element that plays versatile roles in biological systems. One significant function is its involvement in redox reactions found in numerous enzymatic processes.[1−4] While high-valent $Mn^{n+}$-oxo species are well-recognized for their critical function in substrate oxidation reactions,[5−11] midvalent Mn(III)-hydroxo species also play crucial roles in various natural oxidation processes.[10−18] A notable example is manganese superoxide dismutase (MnSOD), which protects cells from oxidative stress by converting superoxide radicals into hydrogen peroxide and molecular oxygen.[12−14] It has been proposed that, in the oxidized form of MnSOD, its active site contains a Mn(III)−OH unit that catalyzes the oxidation of superoxide to dioxygen—an essential step in the superoxide disproportionation reaction. Another intriguing Mn redox enzyme is Mn-lipoxygenase (MnLOX), which also features a Mn(III)−OH unit in its active site. The MnLOX enzyme catalyzes the oxidation of a C−H bond in polyunsaturated fatty acids by abstracting a hydrogen atom, resulting in the dioxygenation of fatty acids and the formation of lipid hydroperoxides.[15−18]

Interestingly, in both MnSOD and MnLOX, the terminal Mn(III)−OH units mediate proton-coupled-electron-transfer (PCET), facilitating substrate oxidation while undergoing reduction to $Mn^{II}$−$OH_2$ species. The importance of these reactions lies in the fact that substrate oxidation occurs without the need for higher-valent manganese oxidation states. In recent years, there has been increasing interest in exploring the reactivity of the midvalent Mn(III)−OH motifs due to their potential applications as mild oxidants in various oxidative transformation reactions.[10,11,19−29]

Several research groups have prepared Mn(III)-OR (R = H, $CH_3$, *etc.*; Chart 1) compounds over the past few years and demonstrated their reactivity in oxidizing X−H substrates (X =

Received: January 4, 2026
Revised: March 18, 2026
Accepted: March 24, 2026
Published: April 3, 2026

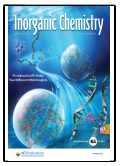


© 2026 American Chemical Society

https://doi.org/10.1021/acs.inorgchem.6c00033
*Inorg. Chem.* 2026, 65, 8465−8480

**Chart 1. Representative Structures of $Mn^{III}$−O(R) Complexes Reported in the Literature: $[Mn^{III}(OH)(PY5)]^{2+}$ (I),[19] $[Mn^{III}(OR)(S^{Me2}N_4(tren))]^{1+}$ ($II^R$),[20] $[Mn^{III}(OH)(dpaq^{SR})]^{1+}$ ($III^R$),[21,25,27] $[Mn^{III}(OH)(pin^F)_2]^{2-}$ (IV),[28] $[Mn^{III}H_3bpuea\text{-}R(O)]^{2-}$ ($V^R$),[38] $[Mn^{III}(OH)(PaPy_2N)]^{1+}$ (VI),[26] $[Mn^{III}(OH)(PaPy_2Q)]^{1+}$ (VII),[26] $[Mn^{III}(OMe)(dpaq)]^{1+}$ (VIII).[22a]**

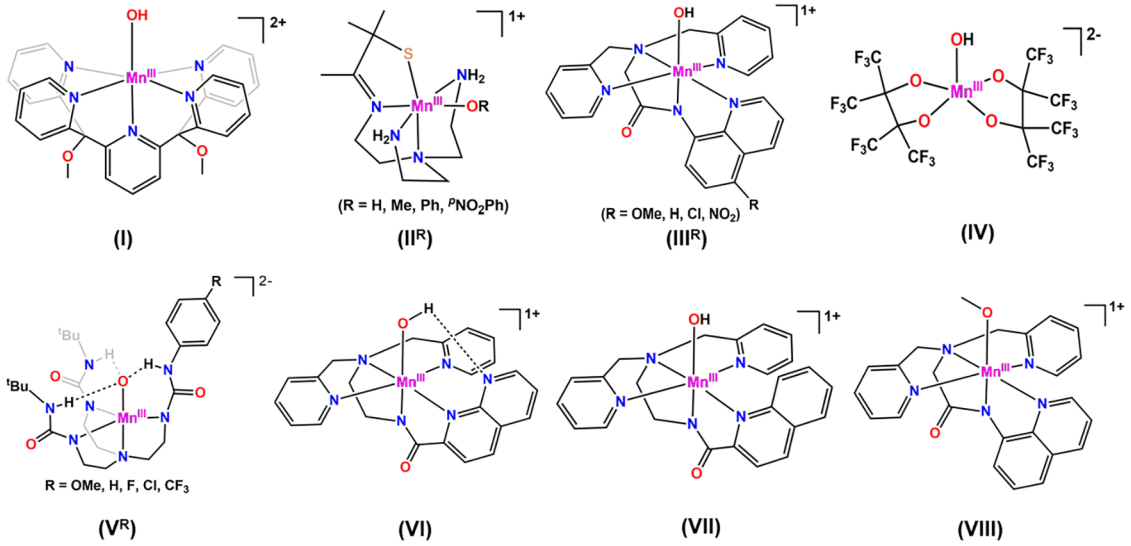


[a]All structures are drawn using the ChemDraw software program.

C/O).[19−29] The activation of these X−H bonds involves a PCET process, where a net hydrogen atom ($H^\bullet = H^+ + e^-$) is transferred from the organic substrate to the Mn(III)-OR unit. During this transfer, the proton binds to the basic OR group bound to the metal, while the electron is transferred to the central Mn(III) ion, resulting in the production of Mn(II)-O(H)R as a metal-based reduced product. This strategy helps prevent the formation of high-valent metal-oxo intermediates during the activation of X−H bonds.

From a thermodynamic perspective, the bond dissociation free energy (BDFE) of the O−H bond in the Mn(II)-O(H)R product should be larger than the BDFE of the X−H bond being broken for efficient hydrogen atom abstraction by the Mn(III)-OR species. The BDFE of the O−H bond in Mn(II)-O(H)R can be correlated with the $Mn^{3+}/Mn^{2+}$ redox potential and the p$K_a$ of the conjugate acid of $Mn^{3+/2+}$-OR, as described in Scheme 1 and the Bordwell equation: $BDFE_{(Mn(II)(RO\text{-}H))} = 23.06E(Mn^{3+}/Mn^{2+}) + 1.37(pK_a) + C_{G,sol}$, where $C_{G,sol}$ is a solvent-dependent constant (*e.g.*, $C_{G,MeOH}$ = 63.4 kcal/mol) that accounts for the formation and solvation of $H^\bullet$ in the solvent.[30,31]

**Scheme 1. Thermodynamic Square Scheme for Proton-Electron Transfer to a $Mn^{III}$−OR/$Mn^{II}$−O(H)R Complex**

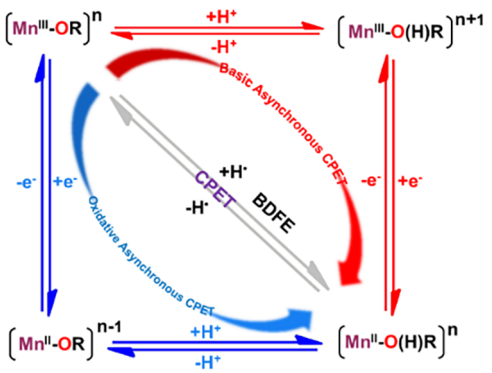


Therefore, the ability of an Mn(III)-OR species to abstract hydrogen atoms is determined by the strength of the O−H bond formed in the Mn(II)-O(H)R product. A higher BDFE of Mn(II)(RO-H) allows the Mn(III)-OR species to efficiently abstract hydrogen from stronger X-H substrates. By manipulating redox potential and acidity parameters through ligand modifications, the BDFE of the O−H bond in Mn(II)-O(H)R can be adjusted according to the Bordwell equation. This relationship provides a basis for designing more efficient Mn(III)-OR oxidants.

Among the "Mn(III)−OH" complexes reported in the literature (Chart 1), Stack's $[Mn^{III}(OH)(PY5)]^{2+}$ (**I**) complex (PY5 = 2,6-bis(bis(2-pyridyl)methoxymethane)-pyridine) is particularly notable for its remarkable reactivity.[19] This complex efficiently cleaves C−H bonds of various strengths, for example, those in xanthene ($BDFE_{C-H}$ = 70.2 kcal/mol in DMSO), 9,10-dihydroanthracene ($BDFE_{C-H}$ = 72.9 kcal/mol in DMSO), fluorene ($BDFE_{C-H}$ = 74.3 kcal/mol in DMSO), and the particularly robust C−H bond in toluene ($BDFE_{C-H}$ = 81.6 kcal/mol in the gas phase).[19,31] The capability of this complex in oxidizing stronger bonds is attributed to the relatively high BDFE of the O−H bond formed in the $[Mn^{II}(OH_2)(PY5)]^{2+}$ product (74.7 kcal/mol in acetonitrile).[31] On the other hand, Kovacs's $[Mn^{III}(OH)(S^{Me2}N_4(tren))]^{1+}$ ($\mathbf{II^H}$) complex[20] ($S^{Me2}N_4$(tren) = 3-((2-(bis(2-aminoethyl)-amino)ethyl)imino-2-methylbutane-2-thiolate) can only break the weak O−H bond of 2,2′,6,6′-tetramethylpiperidine-1-ol (TEMPOH), which has an O−H BDFE of only 66 kcal/mol estimated in MeCN.[31] This subdued reactivity of Kovacs's complex is due to the formation of a weaker O−H bond in the $[Mn^{II}(OH_2)(S^{Me2}N_4(tren))]^{1+}$ product (BDFE of 65.3 kcal/mol in MeCN, recalculated).[20,31] Recently, Jackson and co-workers have developed a mononuclear $[Mn^{III}(OH)(dpaq)]^{1+}$ ($\mathbf{III^H}$) complex[21] (dpaq = 2-(bis(pyridine-2-ylmethyl))amino-*N*-quinolin-8-ylacetamidate) whose hydrogen atom abstraction (HAA) reactivity lies between those of the $[Mn^{III}(OH)(PY5)]^{2+}$ (**I**) and $[Mn^{III}(OH)(S^{Me2}N_4(tren))]^{1+}$ ($\mathbf{II^H}$) complexes. This complex


https://doi.org/10.1021/acs.inorgchem.6c00033
Inorg. Chem. 2026, 65, 8465−8480

was only effective in oxidizing the weak C−H bond of xanthene. However, it could efficiently oxidize various O−H substrates, including TEMPOH and moderate O−H bonds in phenolic compounds like 2,6-di-*tert*-butyl-4-methoxyphenol ($BDFE_{O-H}$ = 72 kcal/mol in MeCN), 2,4,6-tri*tert*-butyl phenol (2,4,6-TTBP, $BDFE_{O-H}$ = 74.8 kcal/mol in MeCN), *etc.*[31] Doerrer et al. recently reported a Mn(III)−OH complex, $[Mn^{III}(OH)(pin^F)_2]^{2-}$ (**IV**), supported by an all-O-donor perfluoropinacolate ligand.[28] This complex could oxidize N−H (1,2-diphenylhydrazine) and O−H (2,4,6-TTBP and TEMPOH) bonds via HAA pathways. The BDFE of the O−H bond in the reduced transient $[Mn^{II}(HO\text{-}H)(pin^F)_2]^{2-}$ species was estimated to be 67−70 kcal/mol in THF.

While the BDFE parameters provide a benchmark for the H atom abstraction ability of Mn(III)-OR complexes, the reactivity rate is influenced by the contributions of the energetics of the electron-transfer and proton-transfer processes to the free energy change of the reaction. In Mn(III)-OR-mediated HAA reactions, the transfer of electron and proton at the respective Mn(III) and OR centers can occur either in a single kinetic step (concerted proton−electron transfer, CPET) or multiple steps (electron transfer followed by proton transfer, or *vice versa*, ET-PT or PT-ET). The CPET process is generally more energetically favorable than the stepwise ET-PT or PT-ET pathways.[32] However, recent studies suggest that CPET can occur nonsynchronously,[33,34] where the transition state may possess either dominant ET (oxidative asynchronous) or PT (basic asynchronous) character.[35] Calculations show that a greater imbalance between ET and PT characteristics in the transition state can reduce the activation barrier more effectively than synchronous processes, leading to a faster rate.[36]

Adjusting redox potential and p$K_a$ are not entirely independent; changing one affects the other in the opposite direction. This reverse relationship between $E_{1/2}$ and p$K_a$ typically counterbalances their impacts on the overall BDFEs. Several strategies have been employed to achieve greater alteration of one parameter over the other between $E_{1/2}$ and p$K_a$, such as modifying primary coordination spheres, altering electronic effects, and regulating secondary coordination sphere interactions (e.g., hydrogen bonds).[20,25−27,37,38] The disparity in the variation of $E_{1/2}$ and p$K_a$ can lead to an imbalanced transition state with either more ET or PT character. This approach has been found effective in accelerating C−H and O−H bond activations. For instance, the HAA reactivity rate of the $[Mn^{III}(OH)(dpaq)]^{1+}$ (**III$^H$**) complex toward substrates with O−H bonds was improved by incorporating electron-withdrawing substituents at the 5-position of the quinoline moiety in the dpaq ligand $\{[Mn^{III}(OH)(dpaq^{5R})]^{1+}$; R = Cl (**III$^{Cl}$**), $NO_2$ (**III$^{NO2}$**)$\}$.[25,27] This improved reactivity with electron-withdrawing groups is due to a larger increase in the $Mn^{III}/Mn^{II}$ redox potential than the p$K_a$ variation, which facilitates the reaction passing through an ET-dominated imbalanced transition state, favoring the oxidative asynchronous mechanism over a balanced CPET pathway.[27] In our previous work, we also observed a similar rate enhancement for the electron-withdrawing groups (OMe < H < Cl < $NO_2$) in C−H bond activation of linoleic acid using $[Fe^{III}(OH)(L^{5R})]^{1+}$ and $[Fe^{III}(OH_2)(L^{5R})]^{2+}$ complexes ($HL^{5R}$ = 2-(((1-methyl-1*H*-imidazol-2-yl)methyl)(pyridin-2-yl-methyl)amino)-*N*-(5-R-quinolin-8-yl)acetamide), following an oxidative asynchronous CPET mechanism.[37]

Tuning the p$K_a$ is also a promising strategy for regulating the HAA reactivity. For example, Borovik and co-workers demonstrated the basicity-controlled mechanism of HAA reactions with their $Mn^{III}$−O complexes, $[Mn^{III}H_3bpuea\text{-}R(O)]^{2-}$ (**V$^R$**; R = OMe, H, Cl, F, $CF_3$, Chart 1).[38] Here, varying R groups from electron-donating to -withdrawing systematically adjusted the basicity of the $Mn^{III}$−O complexes by altering the H-bond strength of the ureayl N−H group with the oxido unit. These $[Mn^{III}H_3bpuea\text{-}R(O)]^{2-}$ complexes activate the C−H bond of 9,10-dihydroanthracene through a PT-dominated CPET mechanism. The reaction rates depend more on changes in the basicity of the $Mn^{III}$−O complexes than on variations in redox potentials. A linear relationship was observed between the reactivity rate and the basicity of the complexes, with the most basic complex (R = OMe) exhibiting the highest rate constant.

Besides modifying the R substituents in the supporting ligand, the $E_{1/2}$ and p$K_a$ values—and hence the reactivity rate—can also be regulated by changing the R group in the Mn(III)-OR unit. This approach has been demonstrated using the series of $[Mn^{III}(OR)(S^{Me2}N_4(tren))]^{1+}$ complexes (**II$^R$**; R = H, Me, Ph, $^pNO_2Ph$) reported by Kovacs's group.[20] In this series, complexes with electron-withdrawing R groups (R = Ph, $^pNO_2Ph$) were inactive in TEMPOH oxidation reactions. In contrast, the Mn(III)-OR complexes with electron-donating R groups (R = H, Me) showed TEMPOH oxidation at comparable rates. The increase in $E_{1/2}$ values for the electron-withdrawing $[Mn^{III}(O^pNO_2Ph)(S^{Me2}N_4(tren))]^{1+}$ and $[Mn^{III}(OPh)(S^{Me2}N_4(tren))]^{1+}$ complexes was insufficient to overcome the extremely low p$K_a$s, which limited their ability to provide the necessary driving force for HAA reactions.

The presence of a H-bond acceptor near the Mn(III)−OH unit has been recognized as another way to enhance reaction rates. Jackson et al. demonstrated this rate-enhancing effect of intramolecular H-bonding within Mn(III)−OH by comparing the reactivity of two related Mn(III)−OH compounds: $[Mn^{III}(OH)(PaPy_2N)]^{1+}$ (**VI**) and $[Mn^{III}(OH)(PaPy_2Q)]^{1+}$ (**VII**).[26] The $[Mn^{III}(OH)(PaPy_2N)]^{1+}$ complex contains a naphthyridinyl moiety that forms an intramolecular H-bond with the OH ligand. In contrast, $[Mn^{III}(OH)(PaPy_2Q)]^{1+}$ lacks an H-bond accepting group in its ligand framework. The $[Mn^{III}(OH)(PaPy_2N)]^{1+}$ complex exhibited substantial rate enhancements in O−H bond oxidations compared to the $[Mn^{III}(OH)(PaPy_2Q)]^{1+}$ complex. This increased reactivity of the $[Mn^{III}(OH)(PaPy_2N)]^{1+}$ complex was attributed to the formation of a stronger O−H bond in the $[Mn^{II}(OH_2)(PaPy_2N)]^{1+}$ product compared to the $[Mn^{II}(OH_2)(PaPy_2Q)]^{1+}$ product. The nitrogen atom in the naphthyridinyl moiety of $[Mn^{II}(OH_2)(PaPy_2N)]^{1+}$ stabilizes the Mn(II)-aqua product through hydrogen bonding, leading to a higher Mn(II)-(HO-H) BDFE and thus increased reactivity.

In addition to the above protocols, another effective method to enhance the oxidizing power of Mn(III)-OR complexes is to use Brønsted acids, which can induce an anodic shift in the $Mn^{III}/Mn^{II}$ redox potential, thereby increasing the reaction rate. Fukuzumi, Nam, and co-workers found that adding triflic acid protonates the hydroxo group of the $[Mn^{III}(OH)(dpaq)]^{1+}$ complex, converting it to the Mn(III)-aqua species $[Mn^{III}(OH_2)(dpaq)]^{2+}$.[39] This Mn(III)-aqua complex exhibits a significantly higher phenolic O−H bond oxidation rate than the Mn(III)-hydroxo complex. The increased oxidizing power of $[Mn^{III}(OH_2)(dpaq)]^{2+}$ is attributed to its substantially


https://doi.org/10.1021/acs.inorgchem.6c00033
Inorg. Chem. 2026, 65, 8465−8480

higher $Mn^{III}/Mn^{II}$ redox potential (1.03 V vs SCE) compared to that of the Mn(III)−OH analog (−0.1 V vs SCE).[39]

Like the Brønsted acids, redox-inactive Lewis-acid metal ions can also modulate the oxidizing power of Mn(III)-OR complexes by interacting with the basic OR site of these complexes. This approach draws inspiration from the $Mn_4CaO_5$ cluster found in the oxygen-evolving complex (OEC) of photosystem II.[40−42] Although the specific role of the $Ca^{2+}$ ion remains unclear, it is believed that $Ca^{2+}$ functions as a Lewis acid and influences the redox reactivity of the manganese oxo cluster to facilitate the catalytic water oxidation reaction.[43,44] Extensive research has been conducted to explore the impact of Lewis/Brønsted acids on the oxidizing properties of higher-valent metal-oxo complexes.[45−55] However, studies with midvalent metal(III)-OR complexes have received less attention. Jackson et al. attempted to evaluate the influence of Lewis-acid salts $Sc(OTf)_3$ and $Al(OTf)_3$ on the reactivity of the $[Mn^{III}(OH)(dpaq)]^{1+}$ ($\mathbf{III^H}$) complex.[56] Their findings, however, indicated that these Lewis acids primarily enhance the Brønsted acidity of the solution, resulting in the protonation of the Mn(III)−OH complex.[56]

In this paper, we aim to elucidate the influence of protonation and Lewis acid binding on the reactivity of M(III)-OR units. To this end, we have synthesized and thoroughly characterized three mononuclear Mn(III) complexes, $[Mn^{III}(L)(MeOH)](ClO_4)$ ($\mathbf{1^{MeOH}(ClO_4)}$), Na-$[Mn^{III}(L)(OMe)](ClO_4)$ ($\mathbf{Na1^{OMe}(ClO_4)}$), and $[Mn^{III}(L)$-$(OMe)]$ ($\mathbf{1^{OMe}}$), supported by a newly designed pentadentate, dianionic $N_4O$ donor ligand, $L^{2-}$ {$H_2L$ = 2-((2-((2-hydroxybenzyl)(methyl)amino)ethyl)(methyl)amino)-*N*-(quinolin-8-yl)acetamide} (Figure 1). Complexes $\mathbf{1^{MeOH+}}$ and

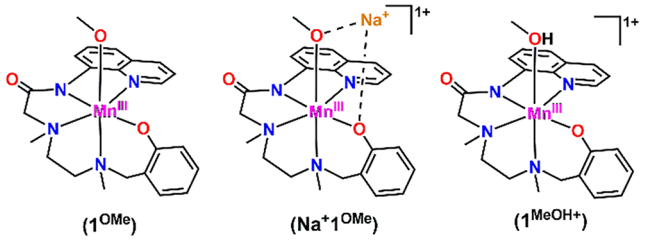


**Figure 1.** ChemDraw representation of the Mn(III) complexes discussed in this work.

$\mathbf{Na^+1^{OMe}}$ have been structurally characterized by X-ray diffraction. The molecular structure of $\mathbf{Na^+1^{OMe}}$ revealed electrostatic interactions between the $Na^+$ ion and the oxygen atom of the methoxide group, as well as with the phenolate oxygen of the ligand. Here, the complex $\mathbf{1^{MeOH+}}$ represents the protonated analog of the methoxide complex $\mathbf{1^{OMe}}$, while $\mathbf{Na^+1^{OMe}}$ is the Lewis-acid adduct of $\mathbf{1^{OMe}}$. We have studied the HAA reactivity of these three Mn(III) complexes with various 4-R-2,6-di-*tert*-butylphenols (4-R-2,6-DTBP; R = OMe, Me, H, Br). All three midvalent Mn(III) complexes effectively oxidize the phenolic substrates, but their reactivity rates vary in the following order: $\mathbf{1^{OMe}} < \mathbf{Na^+1^{OMe}} < \mathbf{1^{MeOH+}}$. Mechanistic analyses suggest that O−H bond activation by these complexes proceeds via an imbalanced CPET mechanism with a predominant ET character, further supported by asynchronicity factor[36] ($\eta$) calculations and ground-state free energy[57] analyses employing Density Functional Theory (DFT) methods. Electrostatic potential mapping[58−62] revealed that $H^+$ or $Na^+$ binding generates an internal positive field, which causes an anodic shift in the $Mn^{III}/Mn^{II}$ potential from complex $\mathbf{1^{OMe}}$ to $\mathbf{Na^+1^{OMe}}$ to $\mathbf{1^{MeOH+}}$. This positive field fine-tunes the oxidative asynchronicity factors, regulating the reactivity order of the complexes.

## RESULTS AND DISCUSSION

### Syntheses and Characterizations

We synthesized a new pentadentate chelating ligand, $H_2L$, through a two-step organic synthesis, as depicted in Scheme S1. The ligand was characterized by $^1H$ and $^{13}C$ NMR spectroscopy (Figures S1 and S2, respectively). In the ESI(+)-MS analysis, a prominent signal was observed at $m/z$ = 379.2328, corresponding to the $[H_2L + H]^+$ molecular ion peak (calculated $m/z$ = 379.2133; Figure S3). The IR spectrum of the ligand shows the respective N−H and C═O stretching bands of the amide group[37] at 3246 $cm^{-1}$ and 1672 $cm^{-1}$ (Figure S4). The phenol C−O stretching vibration appears at 1258 $cm^{-1}$.[63]

We prepared three mononuclear Mn(III) complexes: $[Mn^{III}(L)(MeOH)](ClO_4)$ ($\mathbf{1^{MeOH}(ClO_4)}$), Na$[Mn^{III}(L)$-$(OMe)](ClO_4)$ ($\mathbf{Na1^{OMe}(ClO_4)}$), and $[Mn^{III}(L)(OMe)]$ ($\mathbf{1^{OMe}}$), using the ligand $H_2L$. Reacting $Mn^{II}(ClO_4)_2$ with the deprotonated ligand ($L^{2-}$) in methanol under aerobic conditions produced a green-colored Mn(III) compound, $\mathbf{1^{MeOH}(ClO_4)}$, with a terminal methanol coordination. In this reaction, atmospheric oxygen rapidly oxidizes Mn(II) to Mn(III) (Figure S5). Treating $\mathbf{1^{MeOH}(ClO_4)}$ with one equivalent of NaOMe yielded a brownish-red sodium adduct of Mn(III)-methoxide compound, $\mathbf{Na1^{OMe}(ClO_4)}$. When $Me_4NOH$ was used instead of NaOMe, the Mn(III)-methoxide compound $\mathbf{1^{OMe}}$ was isolated. The molecular formulas of the complexes are determined as follows: $\mathbf{1^{MeOH}(ClO_4)\cdot MeOH}$, $\mathbf{Na1^{OMe}(ClO_4)\cdot 2MeOH}$, and $\mathbf{1^{OMe}\cdot 2MeOH}$, based on CHN analyses. These formulations are further supported by thermogravimetric analysis (TGA). The TG curve of $\mathbf{1^{MeOH}(ClO_4)\cdot MeOH}$ (Figure S6a) shows an initial weight loss of ∼5.5% within the temperature range of 35−80 °C, followed by an additional ∼5.6% weight loss between 80 and 150 °C. The first weight loss corresponds to the release of one lattice methanol molecule (calculated as 5.38%), while the second loss is due to the removal of the coordinated methanol. Further heating leads to a gradual weight loss of about 26% between 200 and 365 °C, indicating partial degradation of the ligand framework, which continues at higher temperatures. The TG curves for $\mathbf{Na1^{OMe}(ClO_4)\cdot 2MeOH}$ and $\mathbf{1^{OMe}\cdot 2MeOH}$ are similar (Figure S6b,c), showing initial weight loss between 35 and 80 °C, which is attributed to the release of two lattice methanol molecules. As the temperature increases, the ligand framework degrades gradually. Energy-dispersive X-ray (EDX) analysis provides the elemental information on the complexes (Figures S7−S9), particularly verifying the presence of sodium in the $\mathbf{Na1^{OMe}(ClO_4)}$ complex.

ESI(+) mass-spectrometry of all three compounds in methanol revealed an intense ion peak at $m/z$ 431.1, corresponding to the monomeric $[Mn(L)]^{1+}$ species (Figure S10).

ATR-FTIR spectra of the solid samples (Figure S11a-c) show strong bands at 1594 $cm^{-1}$ for $\mathbf{1^{MeOH}(ClO_4)\cdot MeOH}$, 1592 $cm^{-1}$ for $\mathbf{Na1^{OMe}(ClO_4)\cdot 2MeOH}$, and 1582 $cm^{-1}$ for $\mathbf{1^{OMe}\cdot 2MeOH}$, attributed to the carbonyl stretching vibrations of the amide group in the ligand.[37] These $\nu(C{=}O)_{amide}$


https://doi.org/10.1021/acs.inorgchem.6c00033
Inorg. Chem. 2026, 65, 8465−8480

stretching frequencies are 78−90 $cm^{-1}$ lower than the free $H_2L$ ligand (1672 $cm^{-1}$). Notably, the $\nu(C{=}O)_{amide}$ band appears at nearly the same position for $\mathbf{1}^{MeOH+}$ and $\mathbf{Na^+1}^{OMe}$ but is about 10 $cm^{-1}$ lower for $\mathbf{1}^{OMe}$ than the $\mathbf{1}^{MeOH+}$ and $\mathbf{Na^+1}^{OMe}$ complexes. The phenolate C−O stretching bands for the Mn(III) complexes are observed between 1270 $cm^{-1}$ and 1280 $cm^{-1}$.[63] Interestingly, the $\nu(C{-}O)_{phenolate}$ band for $\mathbf{Na1}^{OMe}\mathbf{(ClO_4)\cdot 2MeOH}$ is shifted by 9 $cm^{-1}$ to a lower wavenumber (1271 $cm^{-1}$) relative to that of $\mathbf{1}^{OMe}\mathbf{\cdot 2MeOH}$ (1280 $cm^{-1}$) (Figure S11d). The red shift of the $\nu(C{-}O)_{phenolate}$ frequency in $\mathbf{Na1}^{OMe}\mathbf{(ClO_4)\cdot 2MeOH}$ occurs due to the binding of the $Na^+$ ion to the phenolate oxygen, which decreases the double-bond character of the phenolate C−$O^-$ bond induced by resonance. This $Na^+$-phenolate interaction is also observed in the crystal structure of $\mathbf{Na^+1}^{OMe}$ described below. All complexes exhibit broad bands in the 3600−3200 $cm^{-1}$ range, corresponding to methanol's $\nu$(O−H) vibration.[64] Complexes $\mathbf{1}^{MeOH}\mathbf{(ClO_4)\cdot MeOH}$ and $\mathbf{Na1}^{OMe}\mathbf{(ClO_4)\cdot 2MeOH}$ show additional IR bands at ∼1100 $cm^{-1}$ and ∼620 $cm^{-1}$ for $\nu(ClO_4)$ vibrations.[37]

Additionally, we recorded ATR-IR spectra of the Mn(III) complexes in methanol (Figure S12a−c). Interestingly, in the solution phase, the $\nu(C{=}O)_{amide}$ vibrations of the Mn(III) complexes appear at higher wavenumbers (1627 $cm^{-1}$ for $\mathbf{1}^{MeOH}\mathbf{(ClO_4)}$, 1615 $cm^{-1}$ for $\mathbf{Na1}^{OMe}\mathbf{(ClO_4)}$, and 1605 $cm^{-1}$ for $\mathbf{1}^{OMe}$) than their solid-state counterparts. This shift of band positions to higher wavenumbers indicates an increase in the carbonyl bond strength in the amide group, likely due to a lower degree of C=O bond polarization in solution. Like the solid-state spectra, in solution the $\nu(C{-}O)_{phenolate}$ band for $\mathbf{Na1}^{OMe}\mathbf{(ClO_4)}$ appears at a lower wavenumber (1271 $cm^{-1}$) than that of $\mathbf{1}^{OMe}$ (1278 $cm^{-1}$, Figure S12d), indicating that the $Na^+\cdots{}^-O$(phenolate) interaction persists in solution.

The electronic spectrum of $\mathbf{1}^{MeOH+}$ in methanol displays a well-resolved band at $\lambda_{max}$ = 575 nm ($\varepsilon$ = 515 $M^{-1}$ $cm^{-1}$) and a poorly resolved, low-intensity band near 900 nm ($\varepsilon$ = 100 $M^{-1}$ $cm^{-1}$) (Figure S13). We tentatively assign this low-intensity 900 nm band to the d-d transition, which is expected for high-spin $d^4$ octahedral Mn(III) complexes (*vide infra*).[65,66] Complexes $\mathbf{Na^+1}^{OMe}$ and $\mathbf{1}^{OMe}$ exhibit similar absorption spectral features (Figure S14). Each of these complexes shows a broad shoulder near 515 nm ($\varepsilon$ ∼ 440 $M^{-1}$ $cm^{-1}$). Interestingly, $Na^+$ binding induces a red shift of the d-d band in $\mathbf{Na^+1}^{OMe}$ (∼870 nm) relative to $\mathbf{1}^{OMe}$ (∼850 nm) (Figure S15). All three complexes display broad shoulders in the 300−400 nm range with high absorption coefficients ($\varepsilon$ ∼ 4000 $M^{-1}$ $cm^{-1}$). Additionally, the spectra of all complexes show an intraligand electronic transition at 253 nm ($\varepsilon$ > 20,000 $M^{-1}$ $cm^{-1}$).

Further, we calculated the electronic spectra of $\mathbf{1}^{MeOH+}$, $\mathbf{Na^+1}^{OMe}$, and $\mathbf{1}^{OMe}$ complexes using the time-dependent density functional theory (TD-DFT) method (Figures S16−S18). Here, for the optimized structure of $\mathbf{Na^+1}^{OMe}$, we modeled the $Na^+$ ion as binding to the methoxide and phenoxide oxygen atoms of the ligand, with four additional solvent methanol molecules coordinating to $Na^+$ to complete a six-coordinate geometry (*vide infra*). The TD-DFT-predicted spectra of these three Mn(III) complexes feature a prominent band in the ∼400−600 nm region, arising from quinoline-amide and phenolate to Mn(III) charge-transfer transitions, along with a weaker band in the visible to near-IR region (∼750−1100 nm) due to d-d transitions. These calculated spectral features match well with the experimental spectra, with some deviations that fall within the expected error of DFT calculations. Notably, the calculated spectrum of $\mathbf{Na^+1}^{OMe}$ also exhibits a red shift of the d-d band position relative to $\mathbf{1}^{OMe}$, consistent with the experimental observation.

We measured the magnetic susceptibilities of the three Mn(III) compounds at room temperature (300 K) in both solid and solution phases. In the solid state, the effective magnetic moment ($\mu_{eff}$) was found to be 4.85 $\mu_B$ for $\mathbf{1}^{MeOH}\mathbf{(ClO_4)\cdot MeOH}$, 4.86 $\mu_B$ for $\mathbf{Na1}^{OMe}\mathbf{(ClO_4)\cdot 2MeOH}$, and 4.89 $\mu_B$ for $\mathbf{1}^{OMe}\mathbf{\cdot 2MeOH}$. These $\mu_{eff}$ values agree with the expected values for high-spin ($S$ = 2) $d^4$ systems. The solution magnetic moments, measured in $CD_3OD$ using the Evans method (Figure S19), also align with those of high-spin $d^4$ systems, with all three complexes exhibiting values of ∼4.8 $\mu_B$. These solution data suggest that the Mn(III) complexes maintain a monomeric structure in methanol solvent rather than forming antiferromagnetically coupled dimeric "$Mn^{III}$−O−$Mn^{III}$" species, as observed with Jackson's $[Mn^{III}(OH)(dpaq^{5R})]^{1+}$ complexes in dry $CH_3CN$ solvent.[24,25]

Furthermore, we conducted magnetic susceptibility measurements on powder samples of the three Mn(III) complexes over a temperature range from 300 to 10 K. Figure S20 displays the $\chi_M T$ vs $T$ plots for these compounds. We observed a gradual decrease in $\chi_M T$ values for the compounds $\mathbf{1}^{MeOH}\mathbf{(ClO_4)\cdot MeOH}$ and $\mathbf{Na1}^{OMe}\mathbf{(ClO_4)\cdot 2MeOH}$ as the temperature decreased from 300 to 10 K, which likely indicates a thermally induced spin transition process.[67,68] Notably, complex $\mathbf{Na1}^{OMe}\mathbf{(ClO_4)\cdot 2MeOH}$ fully transforms from a high-spin ($S$ = 2) to a low-spin ($S$ = 1) state upon cooling to 10 K. In contrast, complex $\mathbf{1}^{OMe}\mathbf{\cdot 2MeOH}$ remains in the high-spin state across the 300−50 K temperature range. The slight decrease in the $\chi_M T$ values below 50 K may be due to the zero-field splitting effects of the high-spin Mn(III) ion.[67]

We recorded $^1$H NMR data for $\mathbf{1}^{MeOH+}$, $\mathbf{Na^+1}^{OMe}$, and $\mathbf{1}^{OMe}$ complexes at room temperature in $CD_3OD$. The spectrum of each Mn(III) complex exhibits weak and broad signals between +160 and −60 ppm (Figure S21). The observed large chemical shifts and broadening of many signals are consistent with the spectral features reported previously for high-spin paramagnetic mononuclear Mn(III) complexes.[24,25,69]

## Structural Characterizations

**(a) $[Mn^{III}(L)(MeOH)](CF_3SO_3)$ ($\mathbf{1}^{MeOH}\mathbf{(CF_3SO_3)}$).** We determined the structure of $[Mn^{III}(L)(MeOH)](CF_3SO_3)$ using X-ray diffraction (XRD) at 300 K. Figure 2 presents the

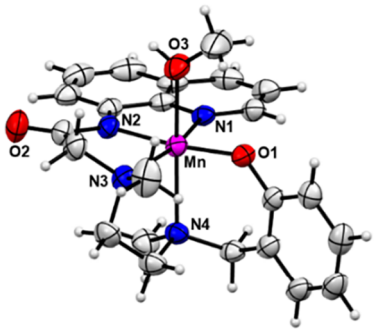


**Figure 2.** ORTEP diagram (30% thermal ellipsoids) of the complex cation in the crystal structure of $[Mn^{III}(L)(MeOH)](CF_3SO_3)$ (CCDC 2393293). The diagram does not show the noncoordinating triflate counteranion.


https://doi.org/10.1021/acs.inorgchem.6c00033
Inorg. Chem. 2026, 65, 8465−8480

ORTEP diagram of the complex cation, and Table 1 lists the important bond lengths and angles. The structure features a

**Table 1. Selected Bond Lengths (Å) and Angles (°) for the Complex Cations $1^{MeOH+}$ and $Na^{+}1^{OMe}$[a]**

| | $1^{MeOH+}$ | $Na^{+}1^{OMe}$ | $\lvert\Delta d\rvert$ |
|---|---|---|---|
| Mn−O1 | 1.842(3) | 1.916(2) | 0.074 |
| Mn−N2 | 1.941(3) | 2.021(2) | 0.080 |
| Mn−N1 | 2.054(3) | 2.231(2) | 0.177 |
| Mn−N3 | 2.147(3) | 2.270(2) | 0.123 |
| Mn−O3 | 2.232(4) | 1.858(2) | 0.374 |
| Mn−N4 | 2.288(4) | 2.179(2) | 0.109 |
| Na−O1 | | 2.471(2) | |
| Na−O3 | | 2.318(2) | |
| O1−Mn−N1 | 95.37(14) | 101.60(7) | |
| N2−Mn−N1 | 81.15(14) | 76.90(7) | |
| O1−Mn−N3 | 103.86(14) | 102.92(7) | |
| N2−Mn−N3 | 80.12(15) | 78.48(7) | |
| O1−Mn−O3 | 85.77(13) | 85.33(6) | |
| N2−Mn−O3 | 89.02(14) | 95.37(7) | |
| N1−Mn−O3 | 94.71(14) | 94.94(8) | |
| N3−Mn−O3 | 91.09(15) | 95.27(8) | |
| O1−Mn−N4 | 88.95(12) | 88.43(6) | |
| N2−Mn−N4 | 96.86(13) | 91.01(7) | |
| N1−Mn−N4 | 95.71(12) | 91.94(8) | |
| N3−Mn−N4 | 80.49(14) | 80.51(8) | |
| O1−Mn−N2 | 173.48(13) | 178.38(6) | |
| N1−Mn−N3 | 160.28(14) | 154.09(6) | |
| O3−Mn−N4 | 168.71(13) | 171.51(6) | |

[a]$\lvert\Delta d\rvert$ values are the absolute differences in the lengths (Å) of the respective bonds between $\mathbf{1}^{MeOH+}$ and $\mathbf{Na^{+}1^{OMe}}$.

six-coordinate Mn(III) center with a distorted octahedral geometry. The ligand $L^{2-}$ provides five donor sites: one quinoline nitrogen (N1), one amide nitrogen (N2), two tertiary amines (N3 and N4), and one phenolate oxygen (O1). The phenolate oxygen (O1) and amide nitrogen (N2) are arranged *trans* to each other, as are the quinoline nitrogen (N1) and the tertiary amine (N3). A methanol ligand occupies the sixth coordination site, *trans* to the N4 tertiary amine donor group. The angles between the *cis*-positioned ligands around the Mn(III) center range from ∼80° to ∼104°, and those between *trans*-positioned ligands span ∼160° to ∼174°, indicating a significant distortion from the ideal octahedral geometry. The O3−Mn−N4 axis, which includes the methanol group and tertiary amine, is elongated [Mn−O3 = 2.232(4) Å, Mn−N4 = 2.288(4) Å]. This elongation results from the Jahn−Teller distortion, a characteristic of high-spin $d^4$ systems. Among the other two axes, the O1−Mn−N2 axis [Mn−O1 = 1.842(3) Å, Mn−N2 = 1.941(3) Å] is somewhat more compressed than the N1−Mn−N3 axis [Mn−N1 = 2.054(3) Å, Mn−N3 = 2.147(3) Å].

**(b) $Na[Mn^{III}(L)(OMe)](ClO_4)$ ($Na1^{OMe}(ClO_4)$).** The XRD structure of the compound reveals that the asymmetric unit contains one $[Mn^{III}(L)(OMe)]$ molecule, one $Na^{+}$ ion, and one perchlorate anion. The Mn(III) center exhibits a distorted octahedral geometry with a methoxide ligand coordinated with it. Structural analysis shows that a $Na^{+}$ ion interacts electrostatically with the O3 atom of the methoxide group and the phenolate oxygen (O1) of the $L^{2-}$ ligand in the crystalline phase. A perspective view of the $\{Na[Mn^{III}(L)(OMe)]\}^{1+}$ unit is shown in Figure 3a. Relevant bond lengths and angles are presented in Table 1. The molecular structure further reveals that the $Na^{+}$ ion interacts with the amide oxygen of a second $\{Na[Mn^{III}(L)(OMe)]\}^{1+}$ unit, forming a one-dimensional (1D) polymeric chain. Examination of the crystal packing diagram shows that two 1D chains are interconnected via interactions between the perchlorate anions and $Na^{+}$, forming a two-dimensional (2D) network (Figure 3b).

The metric parameters (Table 1) for the $\{Na[Mn^{III}(L)(OMe)]\}^{1+}$ unit are consistent with a high-spin Mn(III) center. The $L^{2-}$ ligand binds in the same manner as observed in the $[Mn^{III}(L)(MeOH)]^{1+}$ complex cation, with differences in bond distances and angles. Notably, the Mn(III)-OMe bond (Mn−O3 = 1.858(2) Å) is shorter than the five other Mn(III)-L bonds in the $\{Na[Mn^{III}(L)(OMe)]\}^{1+}$ unit (Table 1). This short Mn(III)-OMe bond length of 1.858(2) Å is comparable to other documented Mn(III)-OMe distances in the literature.[20,22,70] Comparing bond lengths between the $[Mn^{III}(L)(MeOH)]^{1+}$ and $\{Na[Mn^{III}(L)(OMe)]\}^{1+}$ complexes shows that the Mn(III)-O bonds for methanol and methoxide differ by the largest amount, 0.374 Å (Table 1). This significant shortening of the Mn(III)-OMe bond is attributed to the greater donor ability of the negatively charged methoxide ligand compared to methanol. As a result, the O3−Mn−N4 axis is compressed in $\{Na[Mn^{III}(L)(OMe)]\}^{1+}$, and the Jahn−Teller elongation is observed along the N1−Mn−N3 axis, which includes the quinoline nitrogen (N1) and the tertiary amine (N3).

## $^{23}$Na NMR Studies

We recorded the $^{23}$Na NMR spectrum of compound $Na[Mn^{III}(L)(OMe)](ClO_4)$ ($\mathbf{Na1^{OMe}(ClO_4)}$) in $CD_3OD$ and compared it with the spectrum of $NaClO_4$. This study aimed to verify whether the sodium-adduct structure remains intact in the methanol solution. Figure 4a−c depict the $^{23}$Na NMR spectra of NaCl as a reference, $NaClO_4$ salt, and the compound $\mathbf{Na1^{OMe}(ClO_4)}$ in $CD_3OD$. Compound

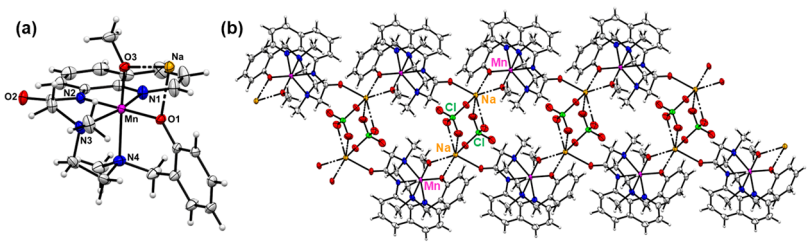


**Figure 3.** (a) ORTEP diagram showing the molecular structure of a single $\{Na[Mn^{III}(L)(OMe)]\}^{1+}$ unit; (b) view of the formation of the 2D network structure in the crystal structure of $Na[Mn^{III}(L)(OMe)](ClO_4)$ (CCDC 2393295). The ellipsoids are drawn at a 30% probability level. Color code: Mn (magenta), Na (orange), Cl (green), O (red), N (blue), C (gray), and H (white).



https://doi.org/10.1021/acs.inorgchem.6c00033
Inorg. Chem. 2026, 65, 8465−8480

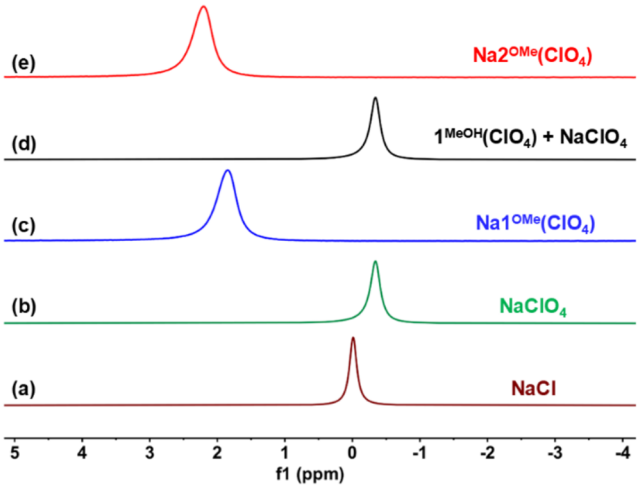


**Figure 4.** $^{23}$Na NMR spectra of (a) NaCl, (b) $NaClO_4$, (c) $Na[Mn^{III}(L)(OMe)](ClO_4)$ (**Na1$^{OMe}$(ClO$_4$)**), (d) 1:1 mixture of $[Mn^{III}(L)(MeOH)](ClO_4)$ (**1$^{MeOH}$(ClO$_4$)**) and $NaClO_4$, and (e) $Na[Co^{III}(L)(OMe)](ClO_4)$ (**Na2$^{OMe}$(ClO$_4$)**) recorded in $CD_3OD$ at 300 K.

**Na1$^{OMe}$(ClO$_4$)** shows a signal at 1.85 ppm in $^{23}$Na NMR, while the signal for $NaClO_4$ appears at −0.35 ppm. Notably, the $^{23}$Na NMR signal of **Na1$^{OMe}$(ClO$_4$)** is broader (FWHM, $\Delta\nu_{1/2}$ = 53.2 Hz) than that of $NaClO_4$ ($\Delta\nu_{1/2}$ = 29.8 Hz). We observed a downfield shift of the $^{23}$Na NMR signal for **Na1$^{OMe}$(ClO$_4$)** relative to $NaClO_4$, indicating a distinct chemical environment for the sodium ion in the compound.

However, this broadening and shift of the $^{23}$Na signal in **Na1$^{OMe}$(ClO$_4$)** compound may also result from the paramagnetic influence of the Mn(III) complex. To investigate this possibility, we recorded the $^{23}$Na NMR spectrum of a 1:1 mixture of $NaClO_4$ and **1$^{MeOH}$(ClO$_4$)** (Figure 4d) to see if the paramagnetic $[Mn^{III}(L)(MeOH)]^{1+}$ species influences the chemical shift and line width of the $^{23}$Na signal in the spectrum. Remarkably, the $Na^+$ ion in this mixture resonates at nearly the same position (−0.34 ppm) and with almost the same line width ($\Delta\nu_{1/2}$ = 29.9 Hz) as that observed for $NaClO_4$ alone (−0.35 ppm, $\Delta\nu_{1/2}$ = 29.8 Hz). These findings suggest that the $Na^+$ ion in the 1:1 mixture retains nearly the same chemical environment as in the pure $NaClO_4$ sample and does not interact with the $[Mn^{III}(L)(MeOH)]^{1+}$ complex. Furthermore, the paramagnetism of $[Mn^{III}(L)(MeOH)]^{1+}$ does not cause any significant shift or broadening of the sodium signal in the $^{23}$Na NMR spectrum of the mixture. This control experiment thus indicates that the downfield shift and line-broadening observed for the $^{23}$Na signal in $Na[Mn^{III}(L)(OMe)](ClO_4)$ do not arise from the paramagnetic influence of the Mn(III) species in solution.

To further strengthen the above interpretation, we measured the $^{23}$Na NMR spectrum of an analogous diamagnetic $Na[Co^{III}(L)(OMe)](ClO_4)$ (**Na2$^{OMe}$(ClO$_4$)**) complex in $CD_3OD$ (Figure 4e). The X-ray crystallographic structure of this cobalt complex (CCDC 2478105) is shown in Figure S22. **Na2$^{OMe}$(ClO$_4$)** exhibits sharp $^1$H NMR signals in the 0 to 10 ppm range, confirming its diamagnetic nature (Figure S23). In the $^{23}$Na NMR, this cobalt complex displays a signal at 2.20 ppm, shifted further downfield relative to the sodium peak in **Na1$^{OMe}$(ClO$_4$)**. The greater downfield shift observed for the sodium signal in the Co(III) compound, compared to that in the Mn(III) analog, is attributed to the higher Lewis acidity of the Co(III) than the Mn(III) ion. Interestingly, the line broadening of the $^{23}$Na signal in **Na2$^{OMe}$(ClO$_4$)** ($\Delta\nu_{1/2}$ = 53.5 Hz) is similar to that in **Na1$^{OMe}$(ClO$_4$)** ($\Delta\nu_{1/2}$ = 53.2 Hz), indicating that the paramagnetism of Mn(III) does not account for the observed line broadening in $Na[Mn^{III}(L)(OMe)](ClO_4)$. We attributed this line-broadening of the $^{23}$Na signal in $Na[Mn^{III}(L)(OMe)](ClO_4)$ to restricted motion of the $Na^+$ ion, likely due to ion-pair formation in solution. The larger size of such an ion-pair can limit molecular motion, leading to faster transverse relaxation and, consequently, signal broadening.

Taken together, these results led us to conclude that the sodium ion indeed exists in an ion-paired form within the $Na[Mn^{III}(L)(OMe)](ClO_4)$ complex in solution. We propose that $Na^+$ preferentially interacts with the coordinated methoxide and phenoxide rather than the amide O atom, due to the higher basicity of methoxide than the amide O atom. To support this proposition, we performed DFT calculations to compare the relative stabilities of the two discrete $Na^+$-bound species: one in which $Na^+$ interacts with methoxide and phenoxide, and another in which it interacts with the amide O atom (Figure S24). The results show that the former species is 10.7 kcal/mol more stable than the latter, indicating a thermodynamic preference for $Na^+$ interaction with methoxide and phenoxide. The IR spectroscopic data for complexes **1$^{OMe}$** and **Na$^+$1$^{OMe}$** in methanol solution further support the computational results, which showed a 7 $cm^{-1}$ red shift in the phenolate C−O stretching band in the presence of $Na^+$ (Figure S12d). This red shift confirms the interaction between $Na^+$ and phenolate-O in **Na$^+$1$^{OMe}$** in solution, as discussed above, and suggests that the $Na^+$ ion resides within the methoxide-phenoxide pocket, as observed in the solid-state structure.

## Electrochemistry and p$K_a$ Determination

We investigated the redox properties of complexes **1$^{OMe}$**, **Na$^+$1$^{OMe}$**, and **1$^{MeOH+}$** by measuring their cyclic voltammograms in methanol at 30 °C. The CV diagrams (Figure 5) of these complexes show a quasi-reversible cathodic process with $E_{1/2}$ values of −0.454 V ($\Delta E \sim$ 185 mV) for **1$^{OMe}$**, −0.396 V ($\Delta E \sim$ 186 mV) for **Na$^+$1$^{OMe}$**, and −0.349 V ($\Delta E \sim$ 120 mV) for **1$^{MeOH+}$**, referenced to $Fc^+$/Fc. These redox events are attributed to the reduction of Mn(III) to Mn(II). The $Mn^{III}$/$Mn^{II}$ reduction potential of the **1$^{OMe}$** complex is higher than

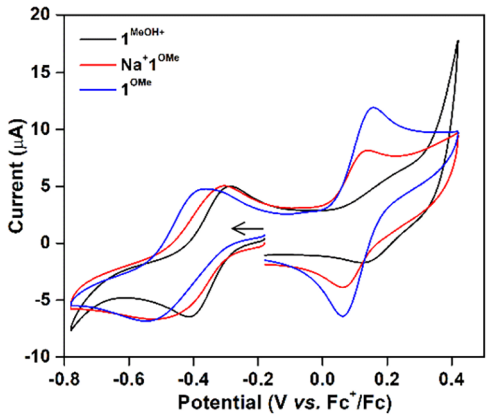


**Figure 5.** Cyclic voltammograms of the complexes **1$^{OMe}$** (blue), **Na$^+$1$^{OMe}$** (red), and **1$^{MeOH+}$** (black) in methanol (scan rate: 100 mV/s).


https://doi.org/10.1021/acs.inorgchem.6c00033
Inorg. Chem. 2026, 65, 8465−8480

that of the analogous $[Mn^{III}(OMe)(dpaq)]^{1+}$ (**VIII**, Chart 1) complex ($E_{pc}$ = −0.88 V vs $Fc^+/Fc$ in MeCN) reported in the literature.[22] Here, we observed an anodic shift in the $Mn^{III}/Mn^{II}$ reduction potential values for $\mathbf{1}^{MeOH+}$ and $\mathbf{Na^+1}^{OMe}$ relative to $\mathbf{1}^{OMe}$, which is expected due to the positive charge that develops when the methoxide ligand in $\mathbf{1}^{OMe}$ undergoes protonation or binds with a $Na^+$ ion. Therefore, the observed anodic shift of the $Mn^{III}/Mn^{II}$ couple for complexes $\mathbf{1}^{MeOH+}$ and $\mathbf{Na^+1}^{OMe}$ indicates that these complexes maintain the apparent solid-state structural integrity in methanol solution (*vide supra*). During the anodic scan, each complex exhibits an oxidative redox response with $E_{1/2}$ values of 0.109 V ($\Delta E \sim 88$ mV) for $\mathbf{1}^{OMe}$, 0.107 V ($\Delta E \sim 80$ mV) for $\mathbf{Na^+1}^{OMe}$, and 0.173 V ($\Delta E \sim 75$ mV) for $\mathbf{1}^{MeOH+}$ vs $Fc^+/Fc$. We assign these redox processes to the formal $Mn^{IV}/Mn^{III}$ couple.

We determined the p$K_a$ of $[Mn^{III}(L)(MeOH)]^{1+}$ by performing a spectrophotometric titration of $[Mn^{III}(L)(OMe)]$ ($\mathbf{1}^{OMe}$) with an organic acid in methanol at 30 °C. Adding pyridinium perchlorate (p$K_a$ = 5.44 in methanol)[71] to a methanol solution of $\mathbf{1}^{OMe}$ produced the protonated analog $[Mn^{III}(L)(MeOH)]^{1+}$ ($\mathbf{1}^{MeOH+}$). We monitored the formation of this protonated species by tracking the gradual increase in absorbance at $\lambda_{max}$ = 575 nm. Figure S25 illustrates the spectral changes for conversion from $\mathbf{1}^{OMe}$ to $\mathbf{1}^{MeOH+}$, showing isosbestic points at 455 and 515 nm. These isosbestic points indicate a clean conversion from $\mathbf{1}^{OMe}$ to $\mathbf{1}^{MeOH+}$. We calculated the p$K_a$ of $[Mn^{III}(L)(MeOH)]^{1+}$ to be 6.67, using the procedure described in the Supporting Information and the plot in Figure S26. Using the redox potential of the $[Mn^{III}(L)(MeOH)]^{1+}/[Mn^{II}(L)(MeOH)]$ couple and the p$K_a$ of $[Mn^{III}(L)(MeOH)]^{1+}$, we estimated the BDFE of $[Mn^{II}(L)(MeO-H)]$ in a methanol solvent to be about 64.5 kcal/mol, according to the Bordwell eq (Scheme 2).[30,31]

**Scheme 2. Thermodynamic Square Scheme for Calculating the BDFE of the O−H Bond in the Coordinated Methanol of $[Mn^{II}(L)(MeO-H)]$**

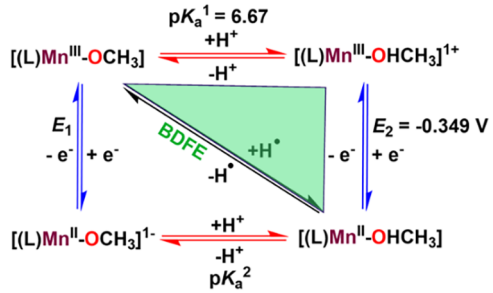


## Oxidation of Phenols

To probe the HAA reactivity of complexes $\mathbf{1}^{OMe}$, $\mathbf{Na^+1}^{OMe}$, and $\mathbf{1}^{MeOH+}$, we conducted reactions with 2,4,6-tri-*tert*-butylphenol (TTBP), a prevalent substrate for studying PCET reactions. After the reactions of these complexes with TTBP in methanol at 30 °C, TTBP was oxidized to 2,4,6-tri-*tert*-butylphenoxyl radical (TTBP•), and Mn(III) complexes were reduced to Mn(II). The products were analyzed using perpendicular-mode X-band EPR spectroscopy. Figure S27 shows a representative EPR spectrum of the product solution from the reaction between $\mathbf{Na^+1}^{OMe}$ and TTBP at a 1:1 molar ratio. The spectrum features a sharp signal at $g \sim 2.0034$, indicative of the phenoxyl radical species,[21] and a six-line signal characteristic of Mn(II) ions.[72] The spin quantification of the $Mn^{II}$ and phenoxyl radical signals, using $Mn(ClO_4)_2$ and TEMPO• as standards, respectively, revealed that the $Mn^{II}$ species and TTBP• were formed in ∼80% yield (Figure S28). Furthermore, when 2,6-di-*tert*-butylphenol was used as a substrate in equal molar ratio with the Mn(III) complexes, a radical coupling product, 3,3′,5,5′-tetra-*tert*-butyl-[1,1′-bi-(cyclohexylidene)]-2,2′,5,5′-tetraene-4,4′-dione, was formed as the major product with 65−80% yield (Figures S29−S31). These findings confirm that all three complexes effectively mediate the PCET process.

In the reactions of the complexes $\mathbf{1}^{OMe}$ and $\mathbf{Na^+1}^{OMe}$ with phenols, the methoxide-O preferentially accepts the proton. As revealed by DFT calculations, the protonation at the methoxide site leads to the formation of the most stable reduced $Mn^{II}$ products (Figures S32−S33). However, in the case of the $\mathbf{1}^{MeOH+}$ complex reacting with phenols, proton transfer is unlikely to occur at the bound methanol. Instead, the phenolate-O or the amidate-N/O within the supporting ligand may serve as the proton acceptor. DFT optimization of the $1e^-/1H^+$ reduced form of the $\mathbf{1}^{MeOH+}$ complex, with a proton attached to either phenolate-O or amidate-N/O, revealed that the protonation at the phenolate-O produced the most stable $Mn^{II}$ product, suggesting that the phenolate-O is the most probable site for protonation in HAA reactions mediated by complex $\mathbf{1}^{MeOH+}$ (Figure S34).

To elucidate the proton−electron transfer mechanism (ET-PT, PT-ET, or CPET), we conducted kinetic studies on the reactions of the complexes $\mathbf{1}^{OMe}$, $\mathbf{Na^+1}^{OMe}$, and $\mathbf{1}^{MeOH+}$ with a series of *para*-substituted 2,6-di-*tert*-butylphenols (4-R-2,6-DTBP), where R varies from electron-donating to electron-withdrawing groups (R = OMe, Me, H, Br). All kinetic experiments were performed under excess-substrate conditions. We monitored the progress of the reactions using UV−vis spectroscopy, tracking the disappearance of the Mn(III) complex bands in the 500−600 nm range over time. Figure 6 illustrates representative UV−vis spectral changes during the Mn(III) to Mn(II) conversion for the reaction between $\mathbf{Na^+1}^{OMe}$ and 4-*H*-2,6-DTBP. The inset in Figure 6 shows the corresponding kinetic time trace, which exhibits nearly first-order exponential decay. We determined the pseudo-first-order rate constants ($k_{obs}$) from the linear fits of the graphs presented in Figures S35−S37. Plots of $k_{obs}$ vs $[4\text{-R-2,6-DTBP}]_0$ display straight lines passing through the origin (Figure S38), and the slope of these lines provides the second-order rate constants

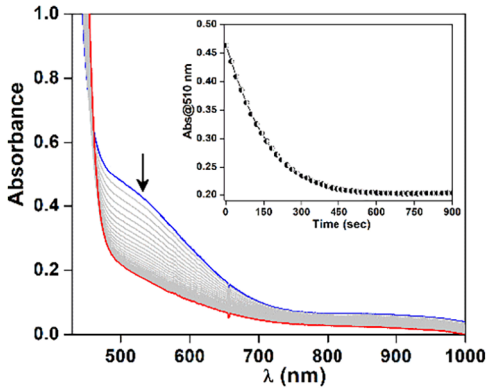


**Figure 6.** Representative UV−vis spectral changes and kinetic time trace (inset) for the reaction of $\mathbf{Na^+1}^{OMe}$ (1 mM) with 2,6-DTBP (40 mM) at 30 °C in methanol.


https://doi.org/10.1021/acs.inorgchem.6c00033
Inorg. Chem. 2026, 65, 8465−8480

($k_2$) listed in Table 2. In this series of Mn(III) complexes, the reactivity trend with each phenol substrate follows the order:

**Table 2. Observed $k_2$ Values for the Reaction of $1^{OMe}$, $Na^+1^{OMe}$, and $1^{MeOH+}$ with Different 4-R-2,6-DTBP Substrates at 30 °C in Methanol**

| Substrate | $BDE_{(phenol\ O-H)}$ (kcal/mol in DMSO)[74] | $k_2$ ($M^{-1}$ $s^{-1}$) | | |
|---|---|---|---|---|
| | | $1^{OMe}$ | $Na^+1^{OMe}$ | $1^{MeOH+}$ |
| 4-OMe-2, 6-DTBP | 78.3 | 1.91(3) | 5.80(8) | 7.20(14) |
| 4-Me-2, 6-DTBP | 81 | 0.098(2) | 0.27(2) | 0.35(1) |
| 4-*H*-2, 6-DTBP | 82 | 0.071(2) | 0.18(1) | 0.22(1) |
| 4-Br-2, 6-DTBP | 83.2 | 0.015(1) | 0.031(1) | 0.035(1) |

$1^{MeOH+}$ > $Na^+1^{OMe}$ > $1^{OMe}$ (Table 2, and Figures 7a, S39). We observed a roughly 2- to 4-fold variation in reaction rates between the highest-performing complex, $1^{MeOH+}$, and the lowest-performing complex, $1^{OMe}$.

It was found that the *para*-substituents of 2,6-DTBP (R = OMe, Me, H, Br) significantly influence the reaction rates. We observed negative Hammett correlations ($\log(k_2^R/k_2^H)$ vs $\sigma_p^+$) for the reaction of 4-R-2,6-DTBP substrates with Mn(III) complexes, with $\rho$ values of −2.07 for $1^{OMe}$, −2.23 for $Na^+1^{OMe}$, and −2.27 for $1^{MeOH+}$. The Hammett plot for the reaction of $1^{MeOH+}$ with 4-R-2,6-DTBP is shown in Figure 7b. The remaining plots are shown in Figure S40. The negative Hammett correlations indicate that reactions of 4-R-2,6-DTBP substrates with Mn(III) complexes are not proton-controlled.[73,74] Therefore, mechanisms such as stepwise PT-ET or basic asynchronous CPET are unlikely, for which a positive Hammett correlation would be expected, as demonstrated previously in the literature.[73,74] The negative $\rho$ value suggests the emergence of a positive charge on the phenolic O−H bond in the transition state,[75] which is consistent with either a stepwise ET-PT or (oxidative asynchronous) CPET mechanism. We measured the $E_{1/2}$ values of the 4-R-2,6-DTBP substrates in methanol using differential pulse voltammetry, obtaining values of 0.309 V (OMe), 0.548 V (Me), 0.696 V (H), and 0.740 V (Br) vs $Fc^+$/Fc (Figure S41). These redox responses are tentatively assigned to $(PhOH)^{\bullet+}$/(PhOH) couples. Notably, the $E_{1/2}$ values of phenols are significantly higher than the complexes' $Mn^{III}/Mn^{II}$ redox potentials. Consequently, the outer-sphere electron transfer from the phenolic O−H bond to the Mn(III) center is thermodynamically nonspontaneous. So, we discard the stepwise ET-PT pathway because the initial ET step is endergonic, thereby suggesting that either a synchronous CPET or an oxidative-asynchronous CPET mechanism is more likely.

We constructed Bell−Evans−Polanyi (BEP) plots to evaluate the reaction pathway by plotting the $\ln(k_2)$ values against the BDE(O−H) of different 4-R-2,6-di-*tert*-butylphenols (BDE = bond dissociation enthalpy).[76] It has previously been demonstrated that the BDEs and BDFEs follow a general linear trend regardless of solvent.[74] Here, we used the BDE values of phenols in our analysis, measured in dimethylsulfoxide (DMSO).[74] Using Ingold's kinetic solvent effect relationship, we calculated the expected rate constants in DMSO from methanol values,[77] as detailed in the Supporting Information. The plot of $\ln(k_2)_{DMSO}$ for phenol oxidation by each Mn(III) complex shows a good linear correlation with the phenol $BDE(O-H)_{DMSO}$ (Figure S42), supporting a common reaction path for all phenols. We converted the slope obtained from the $\ln(k_2)$ vs BDE plot, originally in units of (kcal/mol)$^{-1}$, to a dimensionless parameter, $\alpha$, by multiplying the slope by the thermal energy in kcal/mol ($\alpha$ = slope·RT).[78] This unit less $\alpha$ parameter correlates better with the Gibbs free energy of activation. For the reactions studied, $\alpha$ values are derived as −0.58 for $1^{OMe}$, −0.62 for $Na^+1^{OMe}$, and −0.64 for $1^{MeOH+}$ (Figure S42). These results indicate that the reactions between Mn(III) complexes and phenol substrates proceed via a rate-determining CPET step; however, the slopes deviate slightly from the ideal synchronous CPET slope of −0.5.[79−81] Although the BEP correlations are linear and do not indicate a failure of the conventional rate-driving force relationship, the observed deviations in slope suggest possible asynchronicity. This conclusion, however, is not definitive, given the narrow range of driving forces sampled by the phenol derivatives (∼5 kcal/mol), and thus warrants further analysis using alternative approaches (*vide infra*).

The activation parameters for the hydrogen atom transfer reaction from 4-*H*-2,6-DTBP to Mn(III) complexes were determined using Eyring plots (Figure S43). The $\Delta H^{\ddagger}$ and $\Delta S^{\ddagger}$ values are almost consistent for all three Mn(III) complexes (Table S1), suggesting that they all follow a similar reaction pathway. The large negative $\Delta S^{\ddagger}$ values indicate a well-ordered transition state, which aligns with the CPET mechanism reported in the literature.[21,27,37,82]

We investigated the reactions of $1^{OMe}$, $Na^+1^{OMe}$, and $1^{MeOH+}$ with deuterated 4-*H*-2,6-DTBP-*d*, revealing kinetic isotope

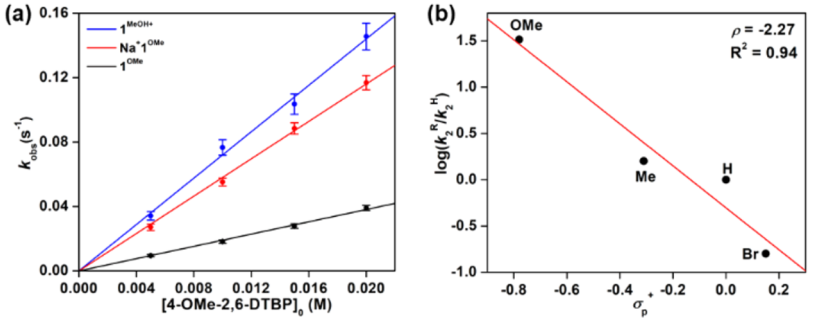


**Figure 7.** (a) A comparative plot of pseudo-first-order rate constants ($k_{obs}$, $s^{-1}$) vs 4-OMe-2,6-DTBP concentrations for HAA reactivity with complexes $1^{OMe}$ (black), $Na^+1^{OMe}$ (red), and $1^{MeOH+}$ (blue); (b) Hammett plot for the reaction of $1^{MeOH+}$ with 4-R-2,6-DTBP substrates (R = OMe, Me, H, Br).



https://doi.org/10.1021/acs.inorgchem.6c00033
Inorg. Chem. 2026, 65, 8465−8480

effect (KIE) values of 1.7, 1.5, and 1.2, respectively. Although these KIE values are small, they suggest that O−H/O−D bond breaking likely occurs in the rate-determining step with a lower tunneling probability. Similar small KIE values (<2) have been observed for O−H bond oxidation mediated by other metal complexes, where O−H/O−D bond cleavage is also considered the rate-limiting step.[21,83] While the hydrogen atom transfer from the phenolic substrates to the Mn(III) complexes appears to be an endergonic process based on bond dissociation energy considerations, the occurrence of the reactions suggests that there may be a fast and thermodynamically favorable follow-up process that drives the phenol oxidation. Product analysis of the reaction between $\mathbf{1}^{\mathbf{MeOH+}}$ and 4-*H*-2,6-DTBP by $^1$H NMR revealed signals corresponding to the protonated free $H_2L$ ligand (Figure S31). In addition, ESI(+)-MS showed an intense signal consistent with the formation of the protonated $H_2L$ ligand for reactions between each Mn(III) complex and 4-*H*-2,6-DTBP (Figures S44−S46). These results suggest that the proton produced from phenols during hydrogen-atom transfer protonates the resulting Mn(II) species, leading to demetalation and ultimately yielding the protonated ligand and Mn(II) salts. These decomposed products are expected to be more stable, so their formation may provide the thermodynamic driving force for phenol oxidation by the Mn(III) complexes. Notably, Stack's $[Mn^{III}(OH)(PY5)]^{2+}$ complex has also been reported to abstract a hydrogen atom from robust toluene, despite the reaction being thermodynamically uphill.[19]

## Marcus-Type Analysis

We performed Marcus-type analysis for the reactions of complexes $\mathbf{1}^{\mathbf{OMe}}$, $\mathbf{Na^+1}^{\mathbf{OMe}}$, and $\mathbf{1}^{\mathbf{MeOH+}}$ with 4-substituted 2,6-di-*tert*-butylphenols to gain a deeper understanding of the mechanism. The plot of $(RT/F)\ln k_2$ against $E_{1/2}$ of 4-R-2,6-DTBP shows a good linear correlation ($R^2 \sim 0.93$) for each Mn(III) complex (Figure 8). This linear free-energy relationship between $(RT/F)\ln k_2$ and $E_{1/2}$ is commonly used to analyze the proton−electron transfer mechanisms involved in the oxidation of phenols.[81−86] According to the Marcus model,[87] a slope value of −0.5 is expected for a pure rate-determining ET process.[81−87] On the other hand, a slope close to 0.0 suggests a balanced CPET mechanism,[81−83] as observed in the oxidation of phenols by cumylperoxyl radical (slope = −0.05).[82,88] For the present complexes, the observed slope values are −0.262 ± 0.052 for $\mathbf{1}^{\mathbf{OMe}}$, −0.282 ± 0.055 for $\mathbf{Na^+1}^{\mathbf{OMe}}$, and −0.286 ± 0.055 for $\mathbf{1}^{\mathbf{MeOH+}}$. These values are less negative than −0.5, indicating that hydrogen-atom transfer from 4-substituted 2,6-DTBP likely occurs via partial charge transfer rather than an ET-PT pathway that involves a complete charge transfer. Moreover, the slopes are not close to 0.0, suggesting that a perfectly balanced CPET mechanism is not fully realized. The deviations from an ideal zero-slope might indicate an imbalanced CPET transition state, in which the ET character dominates the PT, favoring an oxidative asynchronous CPET mechanism.

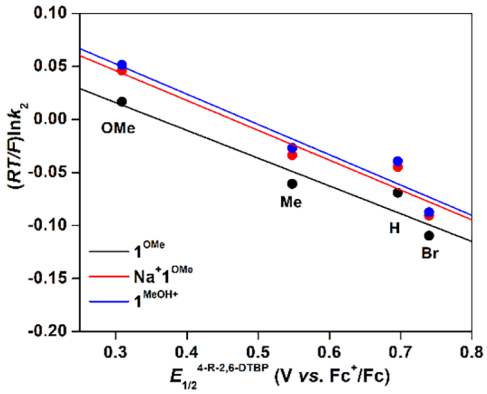


**Figure 8.** Plots of $(RT/F)\ln k_2$ vs substrate (4-R-2,6-DTBP, R = OMe, Me, H, Br) redox potentials ($R^2 \sim 0.93$).

## Electrostatic Potential Mapping

The binding of a proton or Lewis acid primarily generates an internal positive charge,[58−62] which can modulate the reactivity of Mn(III)-complexes by fine-tuning the redox potential and electronic structure of the redox-active Mn(III) center. To illustrate this effect, we performed DFT studies to map the molecular electrostatic potential (ESP) of compounds $\mathbf{1}^{\mathbf{OMe}}$, $\mathbf{Na^+1}^{\mathbf{OMe}}$, and $\mathbf{1}^{\mathbf{MeOH+}}$, as shown in Figure 9. The analysis of these ESP maps reveals that complexes $\mathbf{1}^{\mathbf{MeOH+}}$ and $\mathbf{Na^+1}^{\mathbf{OMe}}$ are significantly more electron-deficient than $\mathbf{1}^{\mathbf{OMe}}$, as indicated by the more positive potential surfaces, shown in red in Figure 9. Among these complexes, $\mathbf{1}^{\mathbf{MeOH+}}$ has the most positive electric field potential. This positive field influences the lowest unoccupied molecular orbital (LUMO) energy of the complexes (Figure S47), decreasing from $\mathbf{1}^{\mathbf{OMe}}$ (−0.63 eV) to $\mathbf{Na^+1}^{\mathbf{OMe}}$ (−0.95 eV) to $\mathbf{1}^{\mathbf{MeOH+}}$ (−1.41 eV) and leading to an anodic shift in the $Mn^{III}/Mn^{II}$ redox potential along this series. Interestingly, the observed reactivity trend of these complexes in phenol oxidations ($\mathbf{1}^{\mathbf{MeOH+}} > \mathbf{Na^+1}^{\mathbf{OMe}} > \mathbf{1}^{\mathbf{OMe}}$) aligns with the order of LUMO stability, suggesting that a more stabilized LUMO facilitates electron transfer from the phenol substrate to the redox-active Mn(III) center. However, while this general trend indicates a relationship between LUMO stability and reactivity, the correlation is much weaker than expected for a pure ET process. Figure S48 displays plots of $\log(k_2)$ vs LUMO energy for the Mn(III) complexes in reactions with 4-R-2,6-DTBP, showing poor linear correlations with $R^2$ ranging from 0.78 to 0.82. This poor correlation implies that a pure ET process is not the rate-determining step, suggesting a CPET process. However, the faster reaction rates observed with more electron-deficient complexes point to an asynchronous mechanism with a dominant ET character in the transition state, indicating an oxidative asynchronous CPET process.

## Asynchronicity Factor ($\eta$) Calculations

To further probe the asynchronous CPET mechanism, we analyzed the asynchronicity factor ($\eta$) for the reactions of Mn(III) complexes with 4-R-2,6-DTBP substrates (R = OMe, Me, H, Br), following the procedure developed by Srnec and co-workers.[36] In this method, an $\eta$ value close to zero indicates a balanced CPET reaction. In contrast, a nonzero $\eta$ suggests an imbalance in the contributions of $E_{1/2}$ and $pK_a$, leading to asynchrony in the electron−proton transfer processes. A positive $\eta$ value indicates that the redox potential is the dominant driving force, pointing to oxidative asynchronous CPET.[36,37] On the other hand, a negative $\eta$ suggests that $pK_a$ is the dominant factor, indicating basic asynchronous CPET.[36,57,73]

In our analysis, we first calculated the driving forces for initial proton transfer ($\Delta G_{PT1}$) and initial electron transfer ($\Delta G_{ET1}$) using DFT methods (see computational details in the Supporting Information, Figures S49−S51). Then, from these


https://doi.org/10.1021/acs.inorgchem.6c00033
Inorg. Chem. 2026, 65, 8465−8480

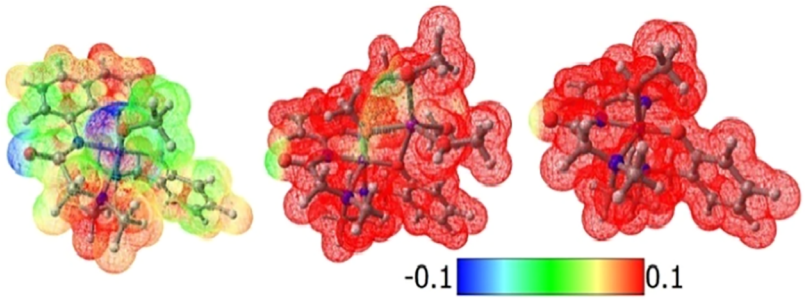


**Figure 9.** Electrostatic potential map for $\mathbf{1}^{\mathbf{OMe}}$ (left), $\mathbf{Na^{+}1}^{\mathbf{OMe}}$ (middle), and $\mathbf{1}^{\mathbf{MeOH+}}$ (right). The color bar indicates the electrostatic potential surface: red represents the most positive potential, and blue represents the most negative potential. The coordination of four additional solvent methanol molecules to the $Na^{+}$ ion has been considered in the $\mathbf{Na^{+}1}^{\mathbf{OMe}}$ complex.

**Table 3. DFT-Calculated $\Delta G_{PT1}$, $\Delta G_{ET1}$, and $\eta$ Values in kcal/mol for Reactions of $\mathbf{1}^{\mathbf{OMe}}$, $\mathbf{Na^{+}1}^{\mathbf{OMe}}$, and $\mathbf{1}^{\mathbf{MeOH+}}$ with Different Phenol Substrates**

| Substrate | $\mathbf{1}^{\mathbf{OMe}}$ | | | $\mathbf{Na^{+}1}^{\mathbf{OMe}}$ | | | $\mathbf{1}^{\mathbf{MeOH+}}$ | | |
|---|---|---|---|---|---|---|---|---|---|
| | $\Delta G_{PT1}$ | $\Delta G_{ET1}$ | $\eta$ | $\Delta G_{PT1}$ | $\Delta G_{ET1}$ | $\eta$ | $\Delta G_{PT1}$ | $\Delta G_{ET1}$ | $\eta$ |
| 4-OMe-2,6-DTBP | 15.42 | 31.12 | −11.10 | 25.70 | 14.44 | 7.96 | 45.54 | 14.58 | 21.89 |
| 4-Me-2,6-DTBP | 13.39 | 36.19 | −16.12 | 24.73 | 19.52 | 3.68 | 44.39 | 19.65 | 17.49 |
| 4-*H*-2,6-DTBP | 13.19 | 41.39 | −19.94 | 24.52 | 24.71 | −0.13 | 44.18 | 24.84 | 13.67 |
| 4-Br-2,6-DTBP | 8.99 | 43.32 | −24.27 | 20.33 | 26.64 | −4.46 | 39.99 | 26.78 | 9.34 |

thermodynamic parameters, $\eta$ values for the HAA reactions of $\mathbf{1}^{\mathbf{OMe}}$, $\mathbf{Na^{+}1}^{\mathbf{OMe}}$, and $\mathbf{1}^{\mathbf{MeOH+}}$ with various phenol substrates were calculated (Table 3). To test the reliability of the computational results, we correlated the calculated $\Delta G_{ET1}$ values with the experimentally determined values. These experimental $\Delta G_{ET1}$ values were derived from the measured redox potentials ($E_{1/2}$) of the corresponding Mn(III) complexes and phenol substrates (Table S2). As shown in Figure S52, the calculated $\Delta G_{ET1}$ values show good linear correlations with the experimental values ($R^2 \sim 0.98$) for all complexes, differing only in absolute magnitude. These correlations demonstrate that, for each Mn(III) complex, the DFT calculations accurately reproduce the experimentally observed trends for this set of phenols. Since p$K_a$s for all complexes and phenol substrates in methanol are not available, experimental $\Delta G_{PT1}$ values could not be determined, and therefore, no correlation with the calculated values was possible.

For $\mathbf{1}^{\mathbf{MeOH+}}$, all $\eta$ values are found to be positive, indicating that HAA reactions proceed via an oxidative asynchronous CPET mechanism. Interestingly, the plot of $(RT)\ln k_2$ vs $\eta$ displays a good linear correlation ($R^2 = 0.94$), with higher asynchronicity corresponding to faster reaction rates (Figure S53). This observation is consistent with Srnec's proposition that greater asynchronicity lowers activation barriers and thereby accelerates reaction rates.[36]

In contrast, for the $\mathbf{Na^{+}1}^{\mathbf{OMe}}$ complex, slightly negative $\eta$ values are obtained with two phenol substrates, while for the $\mathbf{1}^{\mathbf{OMe}}$ complex, negative $\eta$ values are determined for all phenol substrates (Table 3). These negative $\eta$ values may suggest basic asynchronous CPET processes. However, the negative Hammett slopes obtained for both $\mathbf{Na^{+}1}^{\mathbf{OMe}}$ and $\mathbf{1}^{\mathbf{OMe}}$ complexes for reactions with 4-R-2,6-DTBP substrates (Figure S40) rule out the proton-favored asynchronous CPET process.[57,73,74] Moreover, for basic asynchronous mechanisms, reactivity rates are expected to increase with more negative $\eta$ values, according to Srnec's proposition.[36] On the contrary, in our case, the reactivity rates increase with less negative $\eta$ values, showing good linear correlations in the $(RT)\ln(k_2)$ vs $\eta$ plots, with $R^2 \sim 0.92$ for both $\mathbf{Na^{+}1}^{\mathbf{OMe}}$ and $\mathbf{1}^{\mathbf{OMe}}$ (Figures S54 and S55). These findings endorse the oxidative asynchronous CPET mechanisms for both complexes. In addition, the experimental reaction rates show better linear correlations with $\Delta G_{ET1}$ ($R^2 = 0.89-0.93$) than with $\Delta G_{PT1}$ ($R^2 = 0.70-0.82$) for each complex, indicating that the CPET pathways are predominantly ET-controlled in all cases. (Figures S56−S58).

It is worth noting that the asynchronicity factors shift significantly in the positive direction from $\mathbf{1}^{\mathbf{OMe}}$ to $\mathbf{Na^{+}1}^{\mathbf{OMe}}$ to $\mathbf{1}^{\mathbf{MeOH+}}$. The introduction of a positive charge via cation binding makes the initial proton transfer increasingly unfavorable (*i.e.*, $\Delta G_{PT1}$ becomes larger and more positive), leading to a pronounced positive shift in $\eta$ values that drives the reaction toward an oxidatively asynchronous pathway. In our system, protonation induces a more substantial positive shift in asynchronicity than $Na^{+}$ binding. The comparison of electronic spectra between $\mathbf{1}^{\mathbf{OMe}}$ and $\mathbf{Na^{+}1}^{\mathbf{OMe}}$ shows that $Na^{+}$ binding has only a minor effect on the electronic structure of the Mn(III) ion, which implies that the observed positive shift in the asynchronicity factor for $\mathbf{Na^{+}1}^{\mathbf{OMe}}$, relative to $\mathbf{1}^{\mathbf{OMe}}$, is primarily driven by the generation of a positive electrostatic field. Conversely, the protonation of $\mathbf{1}^{\mathbf{OMe}}$ significantly alters the electronic spectrum due to the formation of a covalent O−H bond with the bound OMe group. Therefore, the positive shift in the asynchronicity factor for $\mathbf{1}^{\mathbf{MeOH+}}$ results from a combination of generating a positive charge and modifications in the electronic structure of the Mn(III) ion.

## Analysis of Relative Free Energy Contributions from ET and PT Terms to the Overall Driving Force

While the above experimental and computational results are consistent with an oxidative asynchronous CPET process, we considered further correlating the experimentally observed reactivity rates ($\log k_2$) with a linear combination of free energies associated with the ET and PT terms. For our analysis, we calculated the free energy contributions for the ET ($\Delta G°_{ET1}$) and PT ($\Delta G°_{PT2}$) steps using DFT methods (Supporting Information). This approach deviates from the


https://doi.org/10.1021/acs.inorgchem.6c00033
Inorg. Chem. 2026, 65, 8465−8480

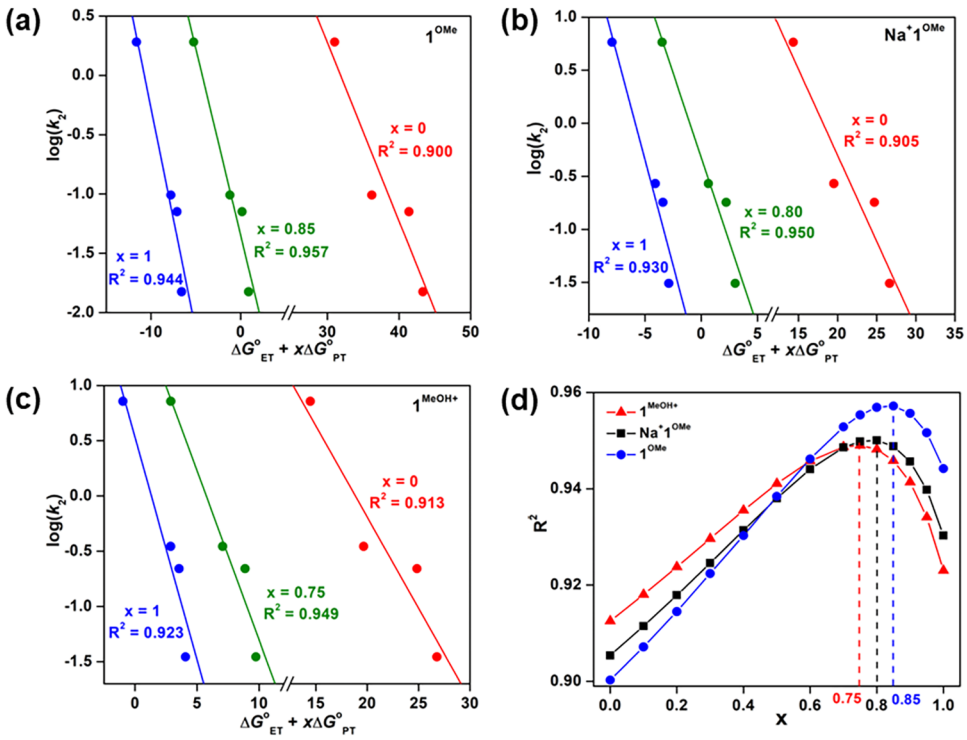


**Figure 10.** Plots of $\log(k_2)$ vs $(\Delta G^{\circ}_{ET} + x\Delta G^{\circ}_{PT})$ for (a) $\mathbf{1}^{\mathbf{OMe}}$, (b) $\mathbf{Na^{+}1}^{\mathbf{OMe}}$, and (c) $\mathbf{1}^{\mathbf{MeOH+}}$, highlighting fittings of reaction rates to ET-driven ($x$ = 0, red), synchronous CPET-driven ($x$ = 1, blue) and ET-dominated imbalanced CPET (olive) mechanisms; (d) plot of $R^2$ vs x for $\mathbf{1}^{\mathbf{OMe}}$ (blue circles), $\mathbf{Na^{+}1}^{\mathbf{OMe}}$ (black squares), and $\mathbf{1}^{\mathbf{MeOH+}}$ (red triangles).

conventional BEP analysis but has proved helpful in distinguishing between synchronous and asynchronous CPET processes, as previously demonstrated by Borovik and co-workers.[57]

In a synchronous CPET process, the electron and proton move simultaneously through the transition state, with $\Delta G^{\circ}_{ET}$ and $\Delta G^{\circ}_{PT}$ terms contributing equally (1:1) to the overall thermodynamic driving force, $\Delta G^{\circ}_{CPET}$ (eq 1). The reaction barrier for synchronous CPET ($\Delta G^{\circ\ddagger}_{syn}$) is linearly related to the driving force $\Delta G^{\circ}_{CPET}$ as given in eq 2.[57]

$$\Delta G^{\circ}_{CPET} = \Delta G^{\circ}_{ET} + \Delta G^{\circ}_{PT} \quad (1)$$

$$\Delta G^{\circ\ddagger}_{syn} = \alpha(\Delta G^{\circ}_{CPET}) + \beta \quad (2)$$

By combining eqs 1 and 2, we derived eq 3, which describes equal weightage of $\Delta G^{\circ}_{ET}$ and $\Delta G^{\circ}_{PT}$ terms in determining changes in the activation barrier.

$$\Delta G^{\circ\ddagger}_{syn} = \alpha(\Delta G^{\circ}_{ET} + \Delta G^{\circ}_{PT}) + \beta \quad (3)$$

Conversely, in the case of an asynchronous CPET process, the electron and proton move at different rates along the reaction coordinates. Consequently, the contributions of ET and PT to the ground-state free energies are not necessarily equivalent. Borovik and co-workers demonstrated that changes in the activation barrier correlate better with a weighted combination of $\Delta G^{\circ}_{ET}$ and $\Delta G^{\circ}_{PT}$ for asynchronous processes.[57] So, for an ET-controlled asynchronous CPET mechanism, we modified eq 3 to obtain eq 4,

$$\Delta G^{\circ\ddagger}_{asyn} = \alpha(\Delta G^{\circ}_{ET} + x\Delta G^{\circ}_{PT}) + \beta \quad (4)$$

where $x$ limits between 0 and 1 ($0 < x < 1$) and $\Delta G^{\circ\ddagger}_{asyn}$ represents the activation barrier for the ET-dominated asynchronous process. A value of $x = 0$ implies a rate-determining ET step followed by PT, while $x = 1$ describes a fully concerted ET-PT process. Any value of $x$ in the range $0 < x < 1$ measures the relative degree of PT character in the ET-dominated CPET mechanism. Combining eq 4 with the Eyring equation provides eq 5[57]

$$\log(k_2) = -\left(\frac{\alpha}{2.303RT}\right)(\Delta G^{\circ}_{ET} + x\Delta G^{\circ}_{PT}) + \beta', \quad (5)$$

where

$$\beta' = \log\left(\frac{\kappa k_B T}{h}\right) - \frac{\beta}{2.303RT}.$$

Equation 5 demonstrates a linear correlation between the reactivity rate $\log(k_2)$ and $(\Delta G^{\circ}_{ET} + x\Delta G^{\circ}_{PT})$. A specific value of $x$ in the range $0 < x < 1$ would provide the best linear fit, which could be determined by evaluating the highest $R^2$ parameter (Figure 10a–c). In Figure 10d, plots of $R^2$ vs $x$ for the three Mn(III) complexes illustrate how the linear fit is affected by the $x$ values. From this analysis, we observed that for all Mn(III) complexes, the best linear correlation was achieved with $x$ values less than 1 ($x$ = 0.85 for $\mathbf{1}^{\mathbf{OMe}}$ with $R^2$ = 0.957, $x$ = 0.80 for $\mathbf{Na^{+}1}^{\mathbf{OMe}}$ with $R^2$ = 0.950, and $x$ = 0.75 for $\mathbf{1}^{\mathbf{MeOH+}}$ with $R^2$ = 0.949), supporting further our assignment for an oxidative asynchronous CPET mechanism. Interestingly, the PT contribution (*i.e.*, the $x$ coefficient) decreases in the order $\mathbf{1}^{\mathbf{OMe}} > \mathbf{Na^{+}1}^{\mathbf{OMe}} > \mathbf{1}^{\mathbf{MeOH+}}$, suggesting that oxidative asynchronicity increases on going from $\mathbf{1}^{\mathbf{OMe}}$ to $\mathbf{Na^{+}1}^{\mathbf{OMe}}$ to $\mathbf{1}^{\mathbf{MeOH+}}$.



https://doi.org/10.1021/acs.inorgchem.6c00033
Inorg. Chem. 2026, 65, 8465−8480

## SUMMARY AND CONCLUSIONS

In the present study, we have described the synthesis and characterization of three novel Mn(III) complexes: $[Mn^{III}(L)(OMe)]$ ($\mathbf{1}^{OMe}$), $\{Na[Mn^{III}(L)(OMe)]\}^{1+}$ ($\mathbf{Na^{+}1^{OMe}}$), and $[Mn^{III}(L)(MeOH)]^{1+}$ ($\mathbf{1}^{MeOH+}$). Complexes $[Mn^{III}(L)(OMe)]$ and $\{Na[Mn^{III}(L)(OMe)]\}^{1+}$ both feature a terminal $Mn^{III}$−OMe unit. In $\{Na[Mn^{III}(L)(OMe)]\}^{1+}$, a $Na^{+}$ ion interacts electrostatically with both the oxygen of the Mn-OMe unit and the phenoxide oxygen of the ligand, forming a Lewis acid $Na^{+}$-adduct. The complex $[Mn^{III}(L)(MeOH)]^{1+}$ with a terminal methanol ligation represents the protonated analog of $[Mn^{III}(L)(OMe)]$. With these protonated and $Na^{+}$-bound compounds in hand, we investigated their hydrogen-atom abstraction reactivity with various 4-R-2,6-di-*tert*-butylphenols (R = OMe, Me, H, Br) and compared them to the reactivity of the reference $\mathbf{1}^{OMe}$ complex. This comparison allowed us to determine how $H^{+}$ or $Na^{+}$ binding affects the HAA reactivity of the Mn(III)-OMe unit. Kinetic studies revealed distinct differences in reaction rates among the complexes. The complex $\mathbf{1}^{MeOH+}$, with the most anodic $Mn^{III}/Mn^{II}$ potential, showed the fastest reactivity, followed by $\mathbf{Na^{+}1^{OMe}}$, and then $\mathbf{1}^{OMe}$, which has the lowest $Mn^{III}/Mn^{II}$ potential in this series. The Hammett analysis of the kinetic data showed that reaction rates decrease with more electron-deficient phenols, exhibiting negative slopes. This negative Hammett correlation is inconsistent with a PT-dominated mechanism. The reaction rates depend on the strength of the O−H bond in phenols. We observed a linear decrease in the reaction rates ($\ln k_2$) with the increase in O−H BDE (BEP plots). These kinetic data, along with large negative activation entropy and mild KIE values (1.2−1.7), support an apparent CPET mechanism for the phenolic O−H bond oxidations by the Mn(III) complexes. However, the Marcus slopes for all three Mn(III) complexes (−0.262 to −0.286) differ substantially from the ideal CPET slope of 0.0, suggesting that the electron−proton transfer does not occur via a synchronous CPET pathway. It is, therefore, reasonable to consider other possibilities, such as asynchronous processes where the electron and proton are transferred unequally at the transition state. For the present reactions, the observed Marcus slopes lie between −0.5 and 0.0, supporting an oxidative asynchronous CPET mechanism, in which the ET character dominates over the PT character.

The binding of $H^{+}$ or $Na^{+}$ generates a positive charge within the molecule, thereby adjusting the LUMO energy and, consequently, the redox potential. Determination of the asynchronicity factor ($\eta$) for the reaction between 4-R-2,6-DTBP and each Mn(III) complex by DFT calculations revealed a gradual positive shift of the $\eta$ value from $\mathbf{1}^{OMe}$ to $\mathbf{Na^{+}1^{OMe}}$ to $\mathbf{1}^{MeOH+}$. These results suggest that developing a positive charge induces greater oxidative-asynchronicity, facilitating electron transfer and accelerating O−H bond-activation reactions. We further validated the ET-dominated asynchronous CPET mechanism by correlating the reactivity rates ($\log k_2$) with the free-energy contributions from the ET and PT terms using Borovik's semiempirical method.

Our studies, therefore, reveal the effect of $H^{+}$ or $Na^{+}$ binding on the HAA reactivity of the midvalent Mn(III)-OMe unit, highlighting the importance of the asynchronicity factor in HAA reactions. Investigation for further improving the oxidizing capacity of metal(III)-OR complexes by developing adducts with stronger Lewis acids (*e.g.*, $K^{+}$, $Ca^{2+}$, $Mg^{2+}$, $Y^{3+}$, *etc.*) and utilizing them to oxidize robust C−H/O−H substrates are underway in our laboratory.

## EXPERIMENTAL SECTION

### Synthesis of Mn(III) Complexes

**$[Mn^{III}(L)(MeOH)](ClO_4)\cdot MeOH$ ($\mathbf{1}^{MeOH}(ClO_4)\cdot MeOH$).** The ligand $H_2L$ (0.100 g, 0.264 mmol) was dissolved in 10 mL of dry methanol. Two equivalents of NaOMe were added, and the mixture was stirred for 10 min. Following this, a 5 mL methanol solution of $Mn(ClO_4)_2$ (0.067 g, 0.264 mmol) was added dropwise, and the solution was stirred for 2 h under aerobic conditions. A color change from yellowish-brown to dark green was observed during the reaction. After that, the solution was filtered, and the volume was reduced to approximately 2−3 mL. Then, 20 mL of diethyl ether was added, yielding green precipitates. The green compound was isolated by filtration, washed three times with diethyl ether, and dried under vacuum. Pure compounds were obtained by recrystallizing from a methanol solution through the slow diffusion of diethyl ether. Yield: 0.080 g (51%). Color: green. Anal. Calcd. for $C_{24}H_{32}ClMnN_4O_8$: C 48.45, H 5.42, N 9.42; Found: C 48.50, H 5.20, N 9.35. ESI(+)-MS (in methanol): $m/z$ 431.1337 (simulated for $C_{22}H_{24}MnN_4O_2$ $[Mn(L)]^{+}$: $m/z$ 431.1279). ATR-FTIR ($cm^{-1}$, solid sample, a few selected bands): 3583−3406 (br, $\nu(OH)_{methanol}$), 1594 ($\nu(C{=}O)_{amide}$), 1271 ($\nu(C{-}O)_{phenolate}$), 1076 and 621 ($\nu(ClO_4)$). ATR-FTIR ($cm^{-1}$, in methanol, a few selected bands): 1627 ($\nu(C{=}O)_{amide}$), 1272 ($\nu(C{-}O)_{phenolate}$), 1100 and 623 ($\nu(ClO_4)$). UV−vis [$\lambda_{max}$, nm ($\varepsilon$, $M^{-1}$ $cm^{-1}$)]: (in methanol) 253 (20170), 365 (sh, 3175), 575 (515), 900 (broad, 100). $\mu_{eff(300\ K)}$ = 4.85 $\mu_B$ (solid state), 4.84 $\mu_B$ (solution state). A triflate salt of the complex, $[Mn^{III}(L)(MeOH)](CF_3SO_3)$, was synthesized via metathesis of $[Mn^{III}(L)(MeOH)](ClO_4)$ with $NaCF_3SO_3$ and characterized by X-ray diffraction.

**$Na[Mn^{III}(L)(OMe)](ClO_4)\cdot 2MeOH$ ($Na\mathbf{1}^{OMe}(ClO_4)\cdot 2MeOH$).** The complex $[Mn^{III}(L)(MeOH)](ClO_4)\cdot MeOH$ (0.100 g, 0.168 mmol) was dissolved in 10 mL of methanol. One equivalent of NaOMe (0.009 g, 0.168 mmol) was added to this solution, and the mixture was stirred at ambient temperature for one hour. During this time, the solution changed from green to a brownish-red. The volume was then reduced to approximately 2−3 mL under reduced pressure. The compound precipitated as a brownish-red solid upon the addition of 20 mL of diethyl ether. The solid was filtered, washed with diethyl ether, and dried in *vacuo*. The compound was dissolved in methanol for recrystallization, and diethyl ether was slowly diffused into the solution, yielding single crystals suitable for X-ray diffraction. Yield: 0.070 g (64%). Color: brownish-red. Anal. Calcd. for $C_{25}H_{35}ClMnN_4NaO_9$: C 46.27, H 5.44, N 8.63; Found: C 46.35, H 5.23, N 8.52. ESI(+)-MS (in methanol): $m/z$ 431.1297 (simulated for $C_{22}H_{24}MnN_4O_2$ $[Mn(L)]^{+}$: $m/z$ 431.1279). ATR-FTIR ($cm^{-1}$, solid sample, a few selected bands): 3587−3382 (br, $\nu(OH)_{methanol}$), 1592($\nu(C{=}O)_{amide}$), 1271 ($\nu(C{-}O)_{phenolate}$), 1083 and 622 ($\nu(ClO_4)$). ATR-FTIR ($cm^{-1}$, in methanol, a few selected bands): 1615 ($\nu(C{=}O)_{amide}$), 1271 ($\nu(C{-}O)_{phenolate}$), 1077 and 621 ($\nu(ClO_4)$). UV−vis [$\lambda_{max}$, nm ($\varepsilon$, $M^{-1}$ $cm^{-1}$)]: (in methanol). 253 (20170), 315 (sh, 4390), 365 (sh, 3700), 515 (sh, 420), 870 (broad, 60). $\mu_{eff(300\ K)}$ = 4.86 $\mu_B$ (solid state), 4.80 $\mu_B$ (solution state).

**$[Mn^{III}(L)(OMe)]\cdot 2MeOH$ ($\mathbf{1}^{OMe}\cdot 2MeOH$).** This complex was synthesized from $[Mn^{III}(L)(MeOH)](ClO_4)\cdot MeOH$ (0.100 g, 0.168 mmol) following a similar procedure to that described for **$Na\mathbf{1}^{OMe}(ClO_4)\cdot 2MeOH$**, but using one equivalent of $Me_4NOH$ as the base instead of NaOMe. Yield: 0.050 g (57%). Color: brownish-red. Anal. Calcd. for $C_{25}H_{35}MnN_4O_5$: C 57.03, H 6.70, N 10.64; Found: C 56.95, H 6.31, N 10.53. ESI(+)-MS (in methanol): $m/z$ 431.1291 (simulated for $C_{22}H_{24}MnN_4O_2$ $[Mn(L)]^{+}$: $m/z$ 431.1279). ATR-FTIR ($cm^{-1}$, solid sample, a few selected bands): 3368−3247 (br, $\nu(OH)_{methanol}$), 1582 ($\nu(C{=}O)_{amide}$), 1280 ($\nu(C{-}O)_{phenolate}$). ATR-FTIR ($cm^{-1}$, in methanol, a few selected bands): 1605 ($\nu(C{=}O)_{amide}$), 1278 ($\nu(C{-}O)_{phenolate}$). UV−vis [$\lambda_{max}$, nm ($\varepsilon$, $M^{-1}$ $cm^{-1}$)]: (in methanol) 253 (20630), 365 (sh, 4250), 515 (sh, 460), 850 (broad, 50). $\mu_{eff(300\ K)}$ = 4.89 $\mu_B$ (solid state), 4.85 $\mu_B$ (solution state).



https://doi.org/10.1021/acs.inorgchem.6c00033
Inorg. Chem. 2026, 65, 8465−8480

## ■ ASSOCIATED CONTENT

### Supporting Information

The Supporting Information is available free of charge at https://pubs.acs.org/doi/10.1021/acs.inorgchem.6c00033.

Materials and reagents, general instrumentation, procedure of ligand synthesis, X-ray diffraction and structure determination methods, kinetic measurements, product analysis, p$K_a$ determination, interconversion of rate constants between different solvents, computational details, characterization data, figures and tables, crystallography table, coordinates for the optimized structures (PDF)

### Accession Codes

Deposition Numbers 2393293, 2393295, and 2478105 contain the supplementary crystallographic data for this paper. These data can be obtained free of charge via the joint Cambridge Crystallographic Data Centre (CCDC) and Fachinformationszentrum Karlsruhe Access Structures service.

## ■ AUTHOR INFORMATION


### Corresponding Author

**Sukanta Mandal** − *Department of Chemistry, Indian Institute of Technology (IIT) Kharagpur, Kharagpur 721302 West Bengal, India;* orcid.org/0000-0001-6456-3898; Email: sukanta.mandal@chem.iitkgp.ac.in

### Authors

**Mofijul Molla** − *Department of Chemistry, Indian Institute of Technology (IIT) Kharagpur, Kharagpur 721302 West Bengal, India*

**Anannya Saha** − *Department of Chemistry, National Institute of Technology (NIT) Agartala, Jirania, Tripura 799046, India*

**Nirmalya Podder** − *Department of Chemistry, Indian Institute of Technology (IIT) Kharagpur, Kharagpur 721302 West Bengal, India*

**Suman K. Barman** − *Department of Chemical Sciences, Indian Institute of Science Education and Research (IISER), Mohali, Manauli 140306, India;* orcid.org/0009-0003-5336-1969

Complete contact information is available at: https://pubs.acs.org/10.1021/acs.inorgchem.6c00033


### Author Contributions

M.M. performed all compound synthesis, characterization, experimental work, kinetic studies, and data analysis. N.P. assisted with the ligand synthesis. A.S. conducted DFT calculations. S.K.B. supervised the theoretical calculations and participated in valuable discussions. S.M. conceptualized, supervised the entire project, and arranged the necessary funds. M.M., A.S., S.K.B., and S.M. contributed to writing the paper.


### Funding

Science and Engineering Research Board (SERB), Government of India (Project No. EMR/2015/001136 to SM), and Council of Scientific and Industrial Research, Government of India (Grant 01(3052)/21/EMR-II to SM).


### Notes

The authors declare no competing financial interest.


## ■ ACKNOWLEDGMENTS

M.M. and N.P. thank IIT Kharagpur for their doctoral fellowships. The Department of Chemistry, Central Research Facility, PARAM SHAKTI computing resources at IIT Kharagpur, and the DST-FIST program (SR/FST/CSII-026/2013) are gratefully acknowledged. M.M. is also grateful to Mr. Rajib Samanta from Prof. T. K. Paine's group at IACS, Kolkata, for his assistance with measuring the paramagnetic NMR and determining the solution magnetic moment of the Mn(III) complexes. The authors acknowledge using AI tools, such as Grammarly and ChatGPT-4.1, to improve the clarity of their English writing. All authors sincerely thank the reviewers for their valuable comments during the revision stage.


## ■ DEDICATION

This paper is dedicated to Prof. Rabindranath Mukherjee.

## ■ REFERENCES


(1) Lawrence, G. D.; Sawyer, D. T. The Chemistry of Biological Manganese. *Coord. Chem. Rev.* **1978**, *27*, 173−193.

(2) Wieghardt, K. The Active Sites in Manganese-Containing Metalloproteins and Inorganic Model Complexes. *Angew. Chem., Int. Ed.* **1989**, *28*, 1153−1172.

(3) Christianson, D. W. Structural Chemistry and Biology of Manganese Metalloenzymes. *Prog. Biophys. Mol. Biol.* **1997**, *67*, 217−252.

(4) McEvoy, J. P.; Brudvig, G. W. Water-Splitting Chemistry of Photosystem II. *Chem. Rev.* **2006**, *106*, 4455−4483.

(5) Wu, X.; Seo, M. S.; Davis, K. M.; Lee, Y.-M.; Chen, J.; Cho, K.-B.; Pushkar, Y. N.; Nam, W. A Highly Reactive Mononuclear Non-Heme Manganese(IV)−Oxo Complex That Can Activate the Strong C−H Bonds of Alkanes. *J. Am. Chem. Soc.* **2011**, *133*, 20088−20091.

(6) Engelmann, X.; Monte-Perez, I.; Ray, K. Oxidation Reactions with Bioinspired Mononuclear Non-Heme Metal−Oxo Complexes. *Angew. Chem. Int. Ed.* **2016**, *55*, 7632−7649.

(7) Sacramento, J. J. D.; Goldberg, D. P. Factors Affecting Hydrogen Atom Transfer Reactivity of Metal−Oxo Porphyrinoid Complexes. *Acc. Chem. Res.* **2018**, *51*, 2641−2652.

(8) Guo, M.; Corona, T.; Ray, K.; Nam, W. Heme and Nonheme High-Valent Iron and Manganese Oxo Cores in Biological and Abiological Oxidation Reactions. *ACS Cent. Sci.* **2019**, *5*, 13−28.

(9) Larson, V. A.; Battistella, B.; Ray, K.; Lehnert, N.; Nam, W. Iron and Manganese Oxo Complexes, Oxo Wall and Beyond. *Nat. Rev. Chem.* **2020**, *4*, 404−419.

(10) Chen, Z.; Yin, G. The Reactivity of the Active Metal Oxo and Hydroxo Intermediates and Their Implications in Oxidations. *Chem. Soc. Rev.* **2015**, *44*, 1083−1100.

(11) Rice, D. B.; Massie, A. A.; Jackson, T. A. Manganese−Oxygen Intermediates in O−O Bond Activation and Hydrogen-Atom Transfer Reactions. *Acc. Chem. Res.* **2017**, *50*, 2706−2717.

(12) Grove, L. E.; Brunold, T. C. Second-Sphere Tuning of the Metal Ion Reduction Potentials in Iron and Manganese Superoxide Dismutases. *Comments Inorg. Chem.* **2008**, *29*, 134−168.

(13) Jackson, T. A.; Gutman, C. T.; Maliekal, J.; Miller, A.-F.; Brunold, T. C. Geometric and Electronic Structures of Manganese-Substituted Iron Superoxide Dismutase. *Inorg. Chem.* **2013**, *52*, 3356−3367.

(14) Sheng, Y.; Abreu, I. A.; Cabelli, D. E.; Maroney, M. J.; Miller, A.-F.; Teixeira, M.; Valentine, J. S. Superoxide Dismutases and Superoxide Reductases. *Chem. Rev.* **2014**, *114*, 3854−3918.

(15) Su, C.; Sahlin, M.; Oliw, E. H. Kinetics of Manganese Lipoxygenase with a Catalytic Mononuclear Redox Center. *J. Biol. Chem.* **2000**, *275*, 18830−18835.

(16) Wennman, A.; Jerneren, F.; Magnuson, A.; Oliw, E. H. Expression and Characterization of Manganese Lipoxygenase of the Rice Blast Fungus Reveals Prominent Sequential Lipoxygenation of α-Linolenic Acid. *Arch. Biochem. Biophys.* **2015**, *583*, 87−95.

(17) Wennman, A.; Oliw, E. H.; Karkehabadi, S.; Chen, Y. Crystal Structure of Manganese Lipoxygenase of the Rice Blast Fungus Magnaporthe oryzae. *J. Biol. Chem.* **2016**, *291*, 8130−8139.
(18) Kostenko, A.; Ray, K.; Iavarone, A. T.; Offenbacher, A. R. Kinetic Characterization of the C−H Activation Step for the Lipoxygenase from the Pathogenic Fungus Magnaporthe oryzae: Impact of N-Linked Glycosylation. *Biochemistry* **2019**, *58*, 3193−3203.
(19) Goldsmith, C. R.; Cole, A. P.; Stack, T. D. P. C−H Activation by a Mononuclear Manganese(III) Hydroxide Complex: Synthesis and Characterization of a Manganese-Lipoxygenase Mimic? *J. Am. Chem. Soc.* **2005**, *127*, 9904−9912.
(20) Coggins, M. K.; Brines, L. M.; Kovacs, J. A. Synthesis and Structural Characterization of a Series of $Mn^{III}OR$ Complexes, Including a Water-Soluble $Mn^{III}OH$ That Promotes Aerobic Hydrogen-Atom Transfer. *Inorg. Chem.* **2013**, *52*, 12383−12393.
(21) Wijeratne, G. B.; Corzine, B.; Day, V. W.; Jackson, T. A. Saturation Kinetics in Phenolic O-H Bond Oxidation by a Mononuclear Mn(III)-OH Complex Derived from Dioxygen. *Inorg. Chem.* **2014**, *53*, 7622−7634.
(22) Wijeratne, G. B.; Day, V. W.; Jackson, T. A. O−H Bond Oxidation by a Monomeric $Mn^{III}$−OMe Complex. *Dalton Trans.* **2015**, *44*, 3295−3306.
(23) Rice, D. B.; Wijeratne, G. B.; Burr, A. D.; Parham, J. D.; Day, V. W.; Jackson, T. A. Steric and Electronic Influence on Proton-Coupled Electron-Transfer Reactivity of a Mononuclear Mn(III)-Hydroxo Complex. *Inorg. Chem.* **2016**, *55*, 8110−8120.
(24) Rice, D. B.; Jones, S. D.; Douglas, J. T.; Jackson, T. A. NMR Studies of a $Mn^{III}$-Hydroxo Adduct Reveal an Equilibrium between $Mn^{III}$-Hydroxo and $\mu$-Oxodimanganese(III,III) Species. *Inorg. Chem.* **2018**, *57*, 7825−7837.
(25) Rice, D. B.; Munasinghe, A.; Grotemeyer, E. N.; Burr, A. D.; Day, V. W.; Jackson, T. A. Structure and Reactivity of ($\mu$-Oxo)Dimanganese(III,III) and Mononuclear Hydroxomanganese-(III) Adducts Supported by Derivatives of an Amide-Containing Pentadentate Ligand. *Inorg. Chem.* **2019**, *58*, 622−636.
(26) Opalade, A. A.; Hessefort, L.; Day, V. W.; Jackson, T. A. Controlling the Reactivity of a Metal-Hydroxo Adduct with a Hydrogen Bond. *J. Am. Chem. Soc.* **2021**, *143*, 15159−15175.
(27) Zhang, J.; Lee, Y.-M.; Seo, M. S.; Kim, Y.; Lee, E.; Fukuzumi, S.; Nam, W. Oxidative versus Basic Asynchronous Hydrogen Atom Transfer Reactions of Mn(III)-Hydroxo and Mn(III)-Aqua Complexes. *Inorg. Chem. Front.* **2022**, *9*, 3233−3243.
(28) Moore, S. M.; Sun, C.; Steele, J. L.; Laaker, E. M.; Rheingold, A. L.; Doerrer, L. H. HAA by the First {Mn(III)OH} Complex with All O-Donor Ligands. *Chem. Sci.* **2023**, *14*, 8187−8195.
(29) Phu, P. N.; Barman, S. K.; Ziller, J. W.; Hendrich, M. P.; Borovik, A. S. Synthesis, Characterization and Reactivity of a Mn(III)−Hydroxido Complex as a Biomimetic Model for Lipoxygenase. *J. Inorg. Biochem.* **2024**, *259*, No. 112618.
(30) Bordwell, F. G.; Cheng, J.-P.; Ji, G.-Z.; Satish, A. V.; Zhang, X. Bond Dissociation Energies in DMSO Related to the Gas Phase Values. *J. Am. Chem. Soc.* **1991**, *113*, 9790−9795.
(31) Agarwal, R. G.; Coste, S. C.; Groff, B. D.; Heuer, A. M.; Noh, H.; Parada, G. A.; Wise, C. F.; Nichols, E. M.; Warren, J. J.; Mayer, J. M. Free Energies of Proton-Coupled Electron Transfer Reagents and Their Applications. *Chem. Rev.* **2022**, *122*, 1−49.
(32) Tyburski, R.; Liu, T.; Glover, S. D.; Hammarstrom, L. Proton-Coupled Electron Transfer Guidelines, Fair and Square. *J. Am. Chem. Soc.* **2021**, *143*, 560−576.
(33) Darcy, J. W.; Kolmar, S. S.; Mayer, J. M. Transition State Asymmetry in C−H Bond Cleavage by Proton-Coupled Electron Transfer. *J. Am. Chem. Soc.* **2019**, *141*, 10777−10787.
(34) Follmer, A. H.; Borovik, A. S. The Role of Basicity in Selective C−H Bond Activation by Transition Metal-Oxidos. *Dalton Trans.* **2023**, *52*, 11005−11016.
(35) Mandal, M.; Elwell, C. E.; Bouchey, C. J.; Zerk, T. J.; Tolman, W. B.; Cramer, C. J. Mechanisms for Hydrogen-Atom Abstraction by Mononuclear Copper(III) Cores: Hydrogen-Atom Transfer or Concerted Proton-Coupled Electron Transfer? *J. Am. Chem. Soc.* **2019**, *141*, 17236−17244.
(36) Bím, D.; Maldonado-Domíngueza, M.; Rulíšek, L.; Srnec, M. Beyond the Classical Thermodynamic Contributions to Hydrogen Atom Abstraction Reactivity. *Proc. Natl. Acad. Sci. U.S.A.* **2018**, *115*, E10287−E10294.
(37) Molla, M.; Saha, A.; Barman, S. K.; Mandal, S. Monomeric Fe (III)-Hydroxo and Fe(III)-Aqua Complexes Display Oxidative Asynchronous Hydrogen Atom Abstraction Reactivity. *Chem. - Eur. J.* **2024**, *30*, No. e202401163.
(38) Barman, S. K.; Jones, J. R.; Sun, C.; Hill, E. A.; Ziller, J. W.; Borovik, A. S. Regulating the Basicity of Metal-Oxido Complexes with a Single Hydrogen Bond and Its Effect on C-H Bond Cleavage. *J. Am. Chem. Soc.* **2019**, *141*, 11142−11150.
(39) Sankaralingam, M.; Lee, Y.-M.; Karmalkar, D. G.; Nam, W.; Fukuzumi, S. A Mononuclear Non-Heme Manganese(III)-Aqua Complex as a New Active Oxidant in Hydrogen Atom Transfer Reactions. *J. Am. Chem. Soc.* **2018**, *140*, 12695−12699.
(40) Umena, Y.; Kawakami, K.; Shen, J. R.; Kamiya, N. Crystal Structure of Oxygen-Evolving Photosystem II at a Resolution of 1.9 Å. *Nature* **2011**, *473*, 55−60.
(41) Suga, M.; Akita, F.; Hirata, K.; Ueno, G.; Murakami, H.; Nakajima, Y.; Shimizu, T.; Yamashita, K.; Yamamoto, M.; Ago, H.; Shen, J.-R. Native Structure of Photosystem II at 1.95 Å Resolution Viewed by Femtosecond X-Ray Pulses. *Nature* **2015**, *517*, 99−103.
(42) Ghosh, A.; Dasgupta, S.; Kundu, A.; Mandal, S. The Impact of Secondary Coordination Sphere Engineering on Water Oxidation Reactivity Catalysed by Molecular Ruthenium Complexes: A Next-Generation Approach to Develop Advanced Catalysts. *Dalton Trans.* **2022**, *51*, 10320−10337.
(43) Tsui, E. Y.; Tran, R.; Yano, J.; Agapie, T. Redox-Inactive Metals Modulate the Reduction Potential in Heterometallic Manganese−Oxido Clusters. *Nat. Chem.* **2013**, *5*, 293−299.
(44) Tsui, E. Y.; Agapie, T. Reduction Potentials of Heterometallic Manganese−Oxido Cubane Complexes Modulated by Redox-Inactive Metals. *Proc. Natl. Acad. Sci. U.S.A.* **2013**, *110*, 10084−10088.
(45) Chen, G.; Ma, L.; Lo, P.-K.; Mak, C.-K.; Lau, K.-C.; Lau, T.-C. Cooperative Activating Effects of Metal Ion and Brønsted Acid on a Metal Oxo Species. *Chem. Sci.* **2021**, *12*, 632−638.
(46) Fukuzumi, S.; Morimoto, Y.; Kotani, H.; Naumov, P.; Lee, Y.-M.; Nam, W. Crystal Structure of a Metal Ion-Bound Oxoiron (IV) Complex and Implications for Biological Electron Transfer. *Nat. Chem.* **2010**, *2*, 756−759.
(47) Park, J.; Morimoto, Y.; Lee, Y.-M.; Nam, W.; Fukuzumi, S. Metal Ion Effect on the Switch of Mechanism from Direct Oxygen Transfer to Metal Ion-Coupled Electron Transfer in the Sulfoxidation of Thioanisoles by a Non-Heme Iron(IV)−Oxo Complex. *J. Am. Chem. Soc.* **2011**, *133*, 5236−5239.
(48) Chen, J.; Lee, Y.-M.; Davis, K. M.; Wu, X.; Seo, M. S.; Cho, K.-B.; Yoon, H.; Park, Y. J.; Fukuzumi, S.; Pushkar, Y. N.; Nam, W. A Mononuclear Non-Heme Manganese(IV)−Oxo Complex Binding Redox-Inactive Metal Ions. *J. Am. Chem. Soc.* **2013**, *135*, 6388−6391.
(49) Codolà, Z.; Gomez, L.; Kleespies, S. T.; Que, L., Jr; Costas, M.; Lloret-Fillol, J. Evidence for an Oxygen Evolving Iron−Oxo−Cerium Intermediate in Iron-Catalysed Water Oxidation. *Nat. Commun.* **2015**, *6*, No. 5865.
(50) Baglia, R. A.; Krest, C. M.; Yang, T.; Leeladee, P.; Goldberg, D. P. High-Valent Manganese−Oxo Valence Tautomers and the Influence of Lewis/Bronsted Acids on C−H Bond Cleavage. *Inorg. Chem.* **2016**, *55*, 10800−10809.
(51) Liu, Y.; Lau, T.-C. Activation of Metal Oxo and Nitrido Complexes by Lewis Acids. *J. Am. Chem. Soc.* **2019**, *141*, 3755−3766.
(52) Sankaralingam, M.; Lee, Y.-M.; Pineda-Galvan, Y.; Karmalkar, D. G.; Seo, M. S.; Jeon, S. H.; Pushkar, Y.; Fukuzumi, S.; Nam, W. Redox Reactivity of a Mononuclear Manganese-Oxo Complex Binding Calcium Ion and Other Redox-Inactive Metal Ions. *J. Am. Chem. Soc.* **2019**, *141*, 1324−1336.


https://doi.org/10.1021/acs.inorgchem.6c00033
*Inorg. Chem.* 2026, 65, 8465−8480

(53) Devi, T.; Lee, Y.-M.; Nam, W.; Fukuzumi, S. Metal Ion-Coupled Electron-Transfer Reactions of Metal-Oxygen Complexes. *Coord. Chem. Rev.* **2020**, *410*, No. 213219.
(54) Gupta, G.; Bera, M.; Paul, S.; Paria, S. Electrochemical Properties and Reactivity Study of $[Mn^{V}(O)(\mu\text{-OR}-\text{Lewis Acid})]$ Cores. *Inorg. Chem.* **2021**, *60*, 18006−18016.
(55) Fukuzumi, S.; Ohkubo, K.; Lee, Y.-M.; Nam, W. Lewis Acid Coupled Electron Transfer of Metal−Oxygen Intermediates. *Chem.-Eur. J.* **2015**, *21*, 17548−17559.
(56) Rice, D. B.; Grotemeyer, E. N.; Donovan, A. M.; Jackson, T. A. Effect of Lewis Acids on the Structure and Reactivity of a Mononuclear Hydroxomanganese(III) Complex. *Inorg. Chem.* **2020**, *59*, 2689−2700.
(57) Barman, S. K.; Yang, M.-Y.; Parsell, T. H.; Green, M. T.; Borovik, A. S. Semiempirical Method for Examining Asynchronicity in Metal−Oxido-Mediated C−H Bond Activation. *Proc. Natl. Acad. Sci. U.S.A.* **2021**, *118*, No. e2108648118.
(58) Reath, A. H.; Ziller, J. W.; Tsay, C.; Ryan, A. J.; Yang, J. Y. Redox Potential and Electronic Structure Effects of Proximal Nonredox Active Cations in Cobalt Schiff Base Complexes. *Inorg. Chem.* **2017**, *56*, 3713−3718.
(59) Kang, K.; Fuller, J.; Reath, A. H.; Ziller, J. W.; Alexandrova, A. N.; Yang, J. Y. Installation of Internal Electric Fields by Non-Redox Active Cations in Transition Metal Complexes. *Chem. Sci.* **2019**, *10*, 10135−10142.
(60) Ghosh, T. K.; Maity, S.; Ghosh, S.; Gomila, R. M.; Frontera, A.; Ghosh, A. Role of Redox-Inactive Metal Ions in Modulating the Reduction Potential of Uranyl Schiff Base Complexes: Detailed Experimental and Theoretical Studies. *Inorg. Chem.* **2022**, *61*, 7130−7142.
(61) Wei, Y.; Zhao, L.; Yuan, R.; Xue, Z.; Mack, J.; Chiyumba, C.; Nyokong, T.; Zhang, J. Promotion of Catalytic Oxygen Reduction Reactions: The Utility of Proton Management Substituents on Cobalt Porphyrins. *Inorg. Chem.* **2022**, *61*, 13085−13095.
(62) Siddiqui, S. A.; Stuyver, T.; Shaik, S.; Dubey, K. D. Designed Local Electric Fields− Promising Tools for Enzyme Engineering. *JACS Au* **2023**, *3*, 3259−3269.
(63) Pinchas, S. The C-O stretching frequency of hydrated isotopic phenolate ions. *Spectrochim. Acta, Part A* **1972**, *28*, 801−802.
(64) Podder, N.; Mandal, S. Aerobic Oxidation of 2-Aminophenol Catalysed by a Series of Mononuclear Copper (II) Complexes: Phenoxazinone Synthase-like Activity and Mechanistic Study. *New J. Chem.* **2020**, *44*, 12793−12805.
(65) Wang, Y.-T.; Xu, P.-Y.; Yu, Z.-M.; Wang, Z.-K.; Wu, H.-Y.; Wang, S.; Li, Y.-H. Solid-State Lattice Effects on High-Spin Mn (III) Complexes with Hexadentate Schiff-Base Ligand. *Supramolecular Chem.* **2021**, *33*, 380−389.
(66) Strassner, N. M.; Stipurin, S.; Koželj, P.; Grin, Y.; Strassner, T. Electronic Structure and Magnetic Properties of a High-Spin $Mn^{III}$ Complex: $[Mn(mesacac)_3]$ (mesacac = 1,3-Bis(2,4,6-trimethylphenyl)-propane-1,3-dionato). *ChemPhysChem* **2023**, *24*, No. e202200652.
(67) Zhao, S.-Z.; Yu, Z.-M.; Qin, C.-Y.; Xu, P.-Y.; Wang, Y.-T.; Li, Y.-H.; Wang, S. Gradual Two-Step and Room Temperature Spin Crossover in Mn(III) Complexes with Nitro-Substituted Ligand. *Inorg. Chim. Acta* **2022**, *538*, No. 120976.
(68) Kühne, I. A.; Ozarowski, A.; Sultan, A.; Esien, K.; Carter, A. B.; Wix, P.; Casey, A.; Heerah-Booluck, M.; Keene, T. D.; Müller-Bunz, H.; Felton, S.; Hill, S.; Morgan, G. G. Homochiral $Mn^{3+}$ Spin-Crossover Complexes: A Structural and Spectroscopic Study. *Inorg. Chem.* **2022**, *61*, 3458−3471.
(69) Ciringh, Y.; Gordon-Wylie, S. W.; Norman, R. E.; Clark, G. R.; Weintraub, S. T.; Horwitz, C. P. Multinuclear Paramagnetic NMR Spectra and Solid State X-Ray Crystallographic Characterization of Manganese(III) Schiff-Base Complexes. *Inorg. Chem.* **1997**, *36*, 4968−4982.
(70) Ghachtouli, S. E.; Guillot, R.; Aukauloo, A.; Dorlet, P.; Anxolabehere-Mallart, E.; Costentin, C. Hydroxide Ion versus Chloride and Methoxide as an Exogenous Ligand Reveals the Influence of Hydrogen Bonding with Second-Sphere Coordination Water Molecules in the Electron Transfer Kinetics of Mn Complexes. *Inorg. Chem.* **2012**, *51*, 3603−3612.
(71) Rived, F.; Roses, M.; Bosch, E. Dissociation Constants of Neutral and Charged Acids in Methyl Alcohol. The Acid Strength Resolution. *Anal. Chim. Acta* **1998**, *374*, 309−324.
(72) Podder, N.; Mandal, S. The Effects of Metal Cofactors on the Reactivity of Quercetin 2, 4-Dioxygenase: Synthetic Model Studies with M(II)-Complexes (M = Mn, Co, Ni, Cu, Zn) and Assessment of the Regulatory Factors in Catalytic Efficacy. *Dalton Trans.* **2022**, *51*, 17064−17080.
(73) Goetz, M. K.; Anderson, J. S. Experimental Evidence for $pK_a$-Driven Asynchronicity in C−H Activation by a Terminal Co(III)−Oxo Complex. *J. Am. Chem. Soc.* **2019**, *141*, 4051−4062.
(74) Fisher, K. J.; Feuer, M. L.; Lant, H. M. C.; Mercado, B. Q.; Crabtree, R. H.; Brudvig, G. W. Concerted Proton-Electron Transfer Oxidation of Phenols and Hydrocarbons by a High-Valent Nickel Complex. *Chem. Sci.* **2020**, *11*, 1683−1690.
(75) Lansky, D. E.; Goldberg, D. P. Hydrogen Atom Abstraction by a High-Valent Manganese(V)−Oxo Corrolazine. *Inorg. Chem.* **2006**, *45*, 5119−5125.
(76) The $BDFE_{O\text{-}H}$ values for all 4-R-2,6-DTBP (R = OMe, Me, H, Br) substrates in a specific solvent were not found in the literature. So, we used $BDE_{O\text{-}H}$ values of the phenol substrates in DMSO (see ref 74) for our analysis, assuming that the differences between BDFE and BDE values are minimal.
(77) Warren, J. J.; Mayer, J. M. Predicting Organic Hydrogen Atom Transfer Rate Constants Using the Marcus Cross Relation. *Proc. Natl. Acad. Sci. U.S.A.* **2010**, *107*, 5282−5287.
(78) Massie, A. A.; Sinha, A.; Parham, J. D.; Nordlander, E.; Jackson, T. A. Relationship between Hydrogen-Atom Transfer Driving Force and Reaction Rates for an Oxomanganese(IV) Adduct. *Inorg. Chem.* **2018**, *57*, 8253−8263.
(79) Warren, J. J.; Tronic, T. A.; Mayer, J. M. Thermochemistry of Proton-Coupled Electron Transfer Reagents and Its Implications. *Chem. Rev.* **2010**, *110*, 6961−7001.
(80) Mayer, J. M. Understanding Hydrogen Atom Transfer: From Bond Strengths to Marcus Theory. *Acc. Chem. Res.* **2011**, *44*, 36−46.
(81) Wu, T.; MacMillan, S. N.; Rajabimoghadam, K.; Siegler, M. A.; Lancaster, K. M.; Garcia-Bosch, I. Structure, Spectroscopy, and Reactivity of a Mononuclear Copper Hydroxide Complex in Three Molecular Oxidation States. *J. Am. Chem. Soc.* **2020**, *142*, 12265−12276.
(82) Lee, J. Y.; Peterson, R. L.; Ohkubo, K.; Garcia-Bosch, I.; Himes, R. A.; Woertink, J.; Moore, C. D.; Solomon, E. I.; Fukuzumi, S.; Karlin, K. D. Mechanistic Insights into the Oxidation of Substituted Phenols via Hydrogen Atom Abstraction by a Cupric−Superoxo Complex. *J. Am. Chem. Soc.* **2014**, *136*, 9925−9937.
(83) Zaragoza, J. P. T.; Siegler, M. A.; Goldberg, D. P. A Reactive Manganese(IV)−Hydroxide Complex: A Missing Intermediate in Hydrogen Atom Transfer by High-Valent Metal-Oxo Porphyrinoid Compounds. *J. Am. Chem. Soc.* **2018**, *140*, 4380−4390.
(84) Kundu, S.; Miceli, E.; Farquharb, E. R.; Ray, K. Mechanism of Phenol Oxidation by Heterodinuclear Ni Cu Bis ($\mu$-Oxo) Complexes Involving Nucleophilic Oxo Groups. *Dalton Trans.* **2014**, *43*, 4264−4267.
(85) Zaragoza, J. P. T.; Cummins, D. C.; Mubarak, M. Q. E.; Siegler, M. A.; Visser, S. P.; de Goldberg, D. P. Hydrogen Atom Abstraction by High-Valent Fe(OH) versus Mn(OH) Porphyrinoid Complexes: Mechanistic Insights from Experimental and Computational Studies. *Inorg. Chem.* **2019**, *58*, 16761−16770.
(86) Jeon, H.; Kim, J.; Kim, J.; Cho, K.-B.; Hong, S. An End-on Bis($\mu$-Hydroxido) Dimanganese(II,III) Azide Complex for C−H Bond and O−H Bond Activation Reactions. *Chem. Commun.* **2022**, *58*, 4623−4626.
(87) Marcus, R. A.; Sutin, N. Electron Transfers in Chemistry and Biology. *Biochim. Biophys. Acta, Rev. Bioenerg.* **1985**, *811*, 265−322.
(88) Osako, T.; Ohkubo, K.; Taki, M.; Tachi, Y.; Fukuzumi, S.; Itoh, S. Oxidation Mechanism of Phenols by Dicopper−Dioxygen ($Cu_2/O_2$) Complexes. *J. Am. Chem. Soc.* **2003**, *125*, 11027−11033.


https://doi.org/10.1021/acs.inorgchem.6c00033
*Inorg. Chem.* 2026, 65, 8465−8480